

Mid-Infrared Spectroscopic Evidence for AGN Heating Warm Molecular Gas

Erini L. Lambrides,^{1,2*} Andreea O. Petric,² Kirill Tchernyshyov,¹ Nadia L. Zakamska¹
Duncan J. Watts¹

¹ Department of Physics & Astronomy, Johns Hopkins University, Bloomberg Center, 3400 N. Charles St., Baltimore, MD 21218, USA

² Institute for Astronomy, University of Hawaii, 65-1238 Mamalahoa Hwy, Kamuela, Hawaii 96743, USA

Accepted XXX. Received YYY; in original form ZZZ

ABSTRACT

We analyse 2,015 mid-infrared (MIR) spectra of galaxies observed with *Spitzer*'s Infrared Spectrograph, including objects with growing super-massive black holes and objects where most of the infrared emission originates from newly formed stars. We determine if and how accreting super-massive black holes at the centre of galaxies – known as active galactic nuclei (AGN) – heat and ionize their host galaxies' dust and molecular gas. We use four MIR diagnostics to estimate the contribution of the AGN to the total MIR emission. We refer to galaxies whose AGN contribute more than 50 per cent of the total MIR emission as AGN-dominated. We compare the relative strengths of PAH emission features and find that PAH grains in AGN-dominated sources have a wider range of sizes and fractional ionizations than PAH grains in non-AGN dominated sources. We measure rotational transitions of H₂ and estimate H₂ excitation temperatures and masses for individual targets, H₂ excitation temperatures for spectra stacked by their AGN contribution to the MIR, and the H₂ excitation temperature distributions via a hierarchical Bayesian model. We find an average 200 K difference between the excitation temperatures of the H₂S(5) and H₂S(7) pure rotational molecular hydrogen transition pair in AGN-dominated versus non-AGN dominated galaxies. Our findings suggest that AGN impact the interstellar medium of their host galaxies.

Key words: galaxies: active - galaxies: ISM - galaxies: starburst - infrared: galaxies - techniques: spectroscopic - surveys

1 INTRODUCTION

The evolution of central supermassive black holes (SMBHs) appears connected to the histories of the host galaxies that harbour them. Observations suggest that there are SMBHs in all galaxy bulges and their masses are proportional to the masses of the host bulges (see Fabian 2012; Kormendy & Ho 2013; Heckman & Best 2014, for reviews). Furthermore, star-formation and SMBH growth have similar evolutions (see Madau & Dickinson 2014, for a review). Theory suggests that feedback from growing SMBHs/active galactic nuclei (AGN) is able to successfully reproduce the properties of local massive galaxies (see Silk & Mamon 2012, for review), and explain the observed galaxy scaling relations and the quenching of star-formation in massive galaxies (Silk & Rees 1998; Fabian 1999; King 2003; Hopkins et al. 2006; Weinberger et al. 2018).

There is mounting observational evidence for AGN interacting with the gas and dust of their host galaxies. Some AGN appear to ionize the interstellar medium (ISM) up to several kiloparsecs away

from the central black hole (Greene et al. 2011, 2012; Liu et al. 2013; Cresci et al. 2015; Villar-Martín et al. 2016; Karouzos et al. 2016; Wylezalek et al. 2017). Strong radio galaxies have been observed injecting energy into the molecular gas of their host galaxies (e.g. Appleton et al. 2006; Ogle et al. 2010; Nesvadba et al. 2011; Guillard et al. 2012). Molecular outflows have been observed in powerful quasars (Feruglio et al. 2010; Ciccone et al. 2012; Stone et al. 2016). Evidence for feedback effects in host galaxies that harbour lower luminosity AGN has been mixed, but these surveys were on relatively small numbers of AGN (e.g. Petric et al. 2011; Hill & Zakamska 2014; Stierwalt et al. 2014; Petric et al. 2018). In this paper, we use mid-infrared (5.2–38.0 μm) spectra of a sample of 2,015 galaxies, 942 of which are galaxies whose IR emission comes predominantly from the AGN, to investigate the impact of the AGN on the warm molecular gas and dust components of the ISM in their host galaxies.

* E-mail: erini.lambrides@jhu.edu

The ISM fuels star-formation and AGN activity. The primary sources for heating the ISM in AGN host galaxies are newly formed stars and supernovae (e.g. Weedman et al. 1981), AGN (Sanders et al. 1989; Elvis et al. 1994; Elitzur 2012), and old stars (Buat & Deharveng 1988; Rowan-Robinson & Crawford 1989; Sauvage & Thuan 1992, 1994). To estimate the impact AGN have on the ISM, we first estimate how much the AGN contributes to the total mid-infrared (MIR) emission. We use a range of diagnostics developed from studies of normal galaxies, luminous AGN, and luminous infrared galaxies using data from the *Infrared Space Observatory* (Genzel et al. 1998, for a review) and the *Spitzer Space Telescope*'s Infrared Spectrograph (Armus et al. 2007a; Spoon et al. 2007; Petric et al. 2011).

Optical diagnostics (e.g. Baldwin et al. 1981; Kauffmann et al. 2003) can provide distinctions between star-formation (SF) and accretion processes, but are not ideal for objects with significant dust obscuration or for composite objects with both significant AGN and SF activity (Trump et al. 2015). MIR diagnostics are less sensitive to dust obscuration. MIR empirical methods that can be used to disentangle an AGN-dominated from an SF-dominated galaxy include the ratio of the continuum to dust emission features, the relative fluxes of high- to low-ionization emission, and the slope of the MIR continuum. These diagnostics were derived using observations of pure star-formation and pure-AGN samples (Genzel et al. 1998; Laurent et al. 2000; Armus et al. 2006; Smith et al. 2007; Spoon et al. 2007). In this paper we use the 6.2 μm polycyclic aromatic hydrocarbon (PAH) equivalent width, hereafter EQW[PAH 6.2 μm], to quantify AGN activity.

PAHs are organic compounds whose emission features in physics laboratories are similar to MIR features in astronomical spectra (Leger et al. 1989; Allamandola et al. 1989). PAH emission features are ubiquitous in MIR spectra of regions with recent star-formation (Tielens 2005). PAHs radiate through IR fluorescence after being excited by a single ultraviolet photon and may play an important role in the energy balance of the ISM. Several models predict the impact of radiation on the ionization and grain sizes of PAHs (Li & Draine 2001; Draine & Li 2007). Although the relations between the PAH features and their environments are not completely understood (Sadjadi et al. 2015; Zhang & Kwok 2015), empirically we measure low EQW[PAH 6.2 μm] in galaxies with AGN (Smith et al. 2007; Sales et al. 2010). This property is a powerful diagnostic of the AGN's contribution to the MIR emission.

In star-forming galaxies, H_2 and PAH emission are tightly correlated (Roussel et al. 2007). H_2 is the dominant component of the warm, dense, star-forming molecular gas of galaxies. H_2 can be excited through three primary mechanisms: (1) far ultraviolet heating, in which photons radiatively pump the H_2 into its electronically excited states; (2) inelastic collisions, in which collisions maintain the lowest pure rotational levels in thermal equilibrium in regions where the gas density and temperature is high enough; and (3) X-ray heating, in which hard X-ray photons penetrate into UV-opaque zones and radiatively excite H_2 .

In normal galaxies, H_2 is predominantly heated by far-ultraviolet photons in photon-dominated regions (PDRs) (Hollenbach & Tielens 1999). For PDRs with $n_{\text{H}} \gtrsim 10^4 \text{ cm}^{-3}$, collisions maintain the lowest rotational levels ($J \lesssim 5$), keeping the PDRs in thermal equilibrium (Burton et al. 1992). This makes their populations consistent with Boltzmann distributions, which makes the H_2 emission a robust thermal probe. Other sources of H_2 excitation include small-scale shocks (Neufeld et al. 2006), extra-nuclear large-scale shocks from galactic gravitational interactions (Apple-

ton et al. 2006; Cluver et al. 2010; Ogle et al. 2012), and X-ray heating (Roussel et al. 2007).

Some AGN host galaxies appear to have more H_2 emission relative to that of other coolants such as PAHs or [Si II] emission, suggesting that at least some of the H_2 does not originate in PDRs. This may indicate that AGN impact the molecular component of their host's ISM (Rigopoulou et al. 2002; Higdon et al. 2006; Zakamska 2010; Petric et al. 2011; Shipley et al. 2013; Hill & Zakamska 2014). While observational studies have provided evidence of some AGN injecting the additional energy required to heat the molecular gas, the small sample size of these studies makes it difficult to assess whether this scenario is representative. Our large catalogue of AGN resolves this.

In galaxies where the AGN contributes most of the IR emission, there is an excess of warm H_2 emission relative to PAH emission (Rigopoulou et al. 2002). Subsequent studies using *Spitzer*'s Infrared Spectrograph confirmed the trend of excess H_2 emission in Ultra Luminous InfraRed Galaxies (ULIRGs) with IR luminosities above $10^{11} L_{\odot}$, and a subset of slightly less luminous LIRGs (Zakamska 2010; Hill & Zakamska 2014; Stierwalt et al. 2014; Petric et al. 2018). Ogle et al. (2012) find excess H_2 emission in over 30 per cent of their sample of radio galaxies. However, Higdon et al. (2006) analyse a similar sample of ULIRGs, and do not find a relationship between the warm H_2 mass and the *IRAS* 25 to 60 μm flux density ratio (an empirical AGN contribution diagnostic), despite finding an excess of warm H_2 relative to the PAH emission.

In this paper we present H_2 and PAH emission measurements in active galaxies observed with the *Spitzer* IRS low resolution ($R = \lambda/\Delta\lambda \sim 60$) modules. Our sample consists of a wide range of infrared luminosities ($\nu L_{\nu}[24 \mu\text{m}] \sim 10^8\text{--}10^{12} L_{\odot}$), which allows us to test if the H_2 to PAH ratio increases as a function of the AGN's contribution to the total IR emission of the galaxy, and if the temperatures of the warm H_2 are different in AGN host galaxies versus SF dominated galaxies. We use the pure rotational transitions of H_2 observed in the MIR to estimate the masses and temperatures of 100–1000 K molecular gas. We then look for differences between H_2 in AGN-dominated galaxies and H_2 in SF-dominated systems.

In section 2 we describe the data acquisition, reduction, and analysis algorithms. In section 3 we present our AGN selection methods, PAH properties of our sample, and molecular hydrogen properties of our sample. We show a significant difference between the temperatures of the higher H_2 transitions in AGN and SF-dominated systems via three independent analysis methods. In section 4 we discuss the implications of AGN host galaxies containing higher H_2 temperature distributions than galaxies dominated by SF processes, and we summarize our findings in section 5. We use an $h = 0.7$, $\Omega_m = 0.3$, $\Omega_{\Lambda} = 0.7$ cosmology throughout this paper. To evaluate the statistical significance of correlations, we use the Spearman rank test (r_s), and report the probability of a null hypothesis as p_s , the probability of two sets of data being uncorrelated. We use the two-sample Kolmogorov–Smirnov test to evaluate if two underlying distributions come from the same distribution.

2 SAMPLE, DATA, AND MEASUREMENTS

2.1 Data Mining

The Infrared Spectrograph (IRS) aboard the *Spitzer Space Telescope* has four separate modules that cover 5.2–3.8 μm : Short-Low (SL), Short-High (SH), Long-Low (LL), and Long-High (LH)

(Houck et al. 2004). Here we amass spectra obtained with the low resolution modules, SL ($60 < R < 128$) and LL ($57 < R < 126$). Each low-resolution module is divided into two in-line sub-slits (i.e. two spectroscopic orders per module): SL1 ($7.46 \mu\text{m} < \lambda < 14.29 \mu\text{m}$), SL2 ($5.13 \mu\text{m} < \lambda < 14.29 \mu\text{m}$), LL1 ($19.91 \mu\text{m} < \lambda < 39.90 \mu\text{m}$), and LL2 ($13.90 \mu\text{m} < \lambda < 21.27 \mu\text{m}$). Some data contain bonus segments in the first order of each module (SL1 Bonus Segment - $7.3 \mu\text{m} < \lambda < 8.7 \mu\text{m}$ and LL2 bonus segment - $19.4 \mu\text{m} < \lambda < 21.7 \mu\text{m}$).

Each observation has an associated unique identifier, an AORkey, which we used to find the observation within the *Spitzer* mission, including coordinates, observation type, and all other relevant information *Spitzer* releases associated with the object. The *Spitzer Space Telescope* team stores this information from all *Spitzer* observations on the NASA/IPAC Infrared Science Archive (SHA). We begin by mining the abstracts from the accepted cold mission *Spitzer* proposals. We use a technique known as ‘web scraping’ to extract data from websites by parsing the html source of the website. We extract all observing programs that contain the following keywords in their abstract text: AGN, Radio Galaxy, QSO, Quasar, Starburst Galaxy, and ULIRG/LIRG. We use the SHA to retrieve IPAC tables with relevant object and observation information (i.e. coordinates, instrument mode, AORkey, etc.) for every program identification number. For the 439 programs, we find a total of 3,793 AORkeys. This paper focuses only on the low-resolution IRS mode, which includes 2,807 AORkeys. Finally, after acquiring redshifts (which we describe in more detail in subsection 2.3) and only using spectra with detection levels $\geq 3\sigma$, we obtain our final sample of 2,015 targets.

We use the *Spitzer* low-resolution reduced spectra provided by the Combined Atlas of Sources with *Spitzer* IRS Spectra (Lebouteiller et al. 2011, CASSIS). The majority of our sample does not have reduced spectra via the enhanced products of *Spitzer* in the SHA, so we use only the CASSIS reduced spectra for consistency. The CASSIS pipeline handles a variety of different observations via an automatic extraction algorithm that accounts for each signal’s detection quality, as well as its spatial extent. The spectral extraction pipeline performs optimal extraction for point-like sources, and a tapered column extraction for extended sources (defined as being greater than 2 arcmin in spatial extent). The optimal extraction method uses the point spread function profile to weigh the pixels in the spatial profile, while the tapered column extraction integrates the flux in a spectral window that expands with wavelength. The algorithm employed in the CASSIS pipeline approximates an uncertainty σ for each spectrum by finding the maximal average signal-to-noise ratio among the module/order/nod spectra. We show the quality of the spectra in our sample in Figure 1.

2.2 Stitching

In 25 per cent of our spectra, we find a difference between the flux in the spectral region of 13.9 to $14.2 \mu\text{m}$ as measured in the SL and LL data respectively. This is partially due to the different widths of the SL and LL slits: SL1 has a width of 3.7 arcsec and LL2 a width of 10.5 arcsec. This causes different parts of a source to be observed by the two slits. For example, at $z = 0.3$ the two slit widths correspond to physical distances of 16.5 kpc and 46.7 kpc respectively.

We use the overlap region to scale the SL spectra to the LL measurements. The range of redshifts ($0.002 < z < 3.0$) in our sample causes the potential break to occur at different rest-frame wavelengths. We develop automated methods to calculate the nec-

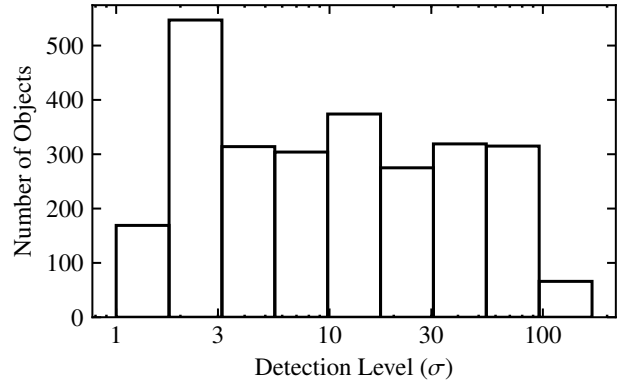


Figure 1. Quality of the sample via CASSIS pipeline: The detection level is the maximal average signal-to-noise ratio among the module/order/nod spectra, and is a data product provided with the reduced spectra. We only use spectra with detection levels $\geq 3\sigma$ and accurate redshift determination, which is discussed in subsection 2.4. This leaves us with 2,015 objects.

essary scalings and account for possible emission features near the overlap region. We use a $1 \mu\text{m}$ window size, centred on the wavelength location of the slit boundaries, to ensure we include enough flux points from each order. We assume the continuum is linear in this small spectral window, then look for and eliminate any emission lines. We then fit a line to the SL and LL overlap separately, estimate the flux from these fits, and estimate a scaling factor to bring the SL overlap emission up to the LL overlap value. To mask out any potential lines in our overlap windows, we proceed as follows. We calculate the forward finite difference for each pair of flux points, i.e. $(f_{v,i+1} - f_{v,i})/\Delta\lambda$, where f_v is the flux density and λ the corresponding wavelength array. We exclude any points whose difference is greater than a standard deviation of the finite difference array. After this step, we perform an additional check by fitting a linear continuum using least squares minimization on each of the spectral segments. If the slopes of the spectral segments are not consistent to within a standard deviation of each segment’s fit, we iteratively remove points until the slope of the line fits this criterion. We provide the resultant scale factors in Table 1.

2.3 Flux Calibration

We test our order stitching algorithm and flux calibration of the CASSIS spectra via a flux comparison to the *Wide-field Infrared Survey Explorer* (*WISE*) fluxes. *WISE* imaged the sky at four wavelengths: 3.4 (*W1*), 4.6 (*W2*), 12 (*W3*), and $22 \mu\text{m}$ (*W4*) with angular resolutions 6.1 , 6.4 , 6.5 and 12 arcsec, respectively (Wright et al. 2010). The IRS SL and LL slits provide complete spectral coverage of the *W3* and *W4* bands respectively. We cross-match our *Spitzer* sample with the *WISE* All-Sky catalogue using the NASA/IPAC Infrared Science Archive (IRSA). We employ a cone search with a tolerance of 6 arcsec to maximize sample overlap while minimizing false matches. We verify that our objects are correctly cross-matched by comparing the coordinates of the associated Two Micron All-Sky Survey (2MASS, Skrutskie et al. 2006) observations where possible (also given in IRSA) and the IRS spectrum coordinates. The 2MASS photometric bands have aperture sizes smaller than that of the *WISE* bands, corresponding to smaller uncertainties in the position of the object. We find complete coverage of *WISE* $22 \mu\text{m}$ photometry for our sample, and 82 per cent of our sample with all *W1*, *W2*, *W3* and *W4* measurements with $S/N > 5$.

Table 1. Example Sample Properties: We list the AORkey (*Spitzer* IRS identification number), RA and Dec, the level of the detection as provided by the CASSIS reduction pipeline, and the cross-matches *WISE* and 2MASS magnitudes. The full version of this table is available in on-line format.

AORkey	RA (deg)	Dec (deg)	Detection (σ)	z	SL1–LL2 Scale	W1 (mag)	W2 (mag)	W3 (mag)	W4 (mag)	J (mag)	H (mag)	K_s (mag)
4935168	186.727	−0.878	109	0.0073	1.126	10.75	9.49	3.89	0.32	13.18	12.45	11.86
6650880	69.961	−48.721	48	0.2035	1	14.15	12.92	8.63	5.64	16.38	15.72	15.00
22115072	139.977	32.933	15	0.0499	1.727	11.29	10.85	6.51	3.84	14.02	13.28	12.79
4671744	186.265	12.887	13	0.0034	1	8.02	8.02	7.14	5.91	10.66	10.05	9.81
4985600	253.245	2.401	109	0.0245	1.097	9.34	8.62	4.53	1.27	11.94	11.20	10.57
22079488	133.908	78.223	29	0.0047	1.987	8.54	8.46	6.38	4.30	10.38	9.55	9.40
18526208	184.740	47.304	42	0.0015	1.250	8.54	8.18	5.48	3.31	11.07	10.54	10.07
25408512	171.848	−29.258	39	0.0239	1.125	10.88	10.54	6.50	3.86	13.67	12.86	12.37
20316160	86.796	17.563	80	0.0186	1.192	10.26	9.79	5.11	2.04	13.16	12.23	11.46
22087680	187.509	13.637	7	0.0045	1.606	8.85	8.91	7.99	6.58	10.69	9.90	10.02

Table 2. Example Molecular Hydrogen Results: We list the AORkey and $\text{H}_2\text{S}(0)$, $\text{H}_2\text{S}(1)$, $\text{H}_2\text{S}(2)$, $\text{H}_2\text{S}(3)$, $\text{H}_2\text{S}(5)$, $\text{H}_2\text{S}(6)$, $\text{H}_2\text{S}(7)$ line luminosities in units of $10^{39} \text{ erg s}^{-1}$ with their respective errors for $\geq 2\sigma$ detections of 10 example objects. For $< 2\sigma$, we only report the upper limit. The full version of this table is available in on-line format.

AORkey	$L[\text{H}_2\text{S}(0)]$ ($10^{39} \text{ erg s}^{-1}$)	$L[\text{H}_2\text{S}(1)]$ ($10^{39} \text{ erg s}^{-1}$)	$L[\text{H}_2\text{S}(2)]$ ($10^{39} \text{ erg s}^{-1}$)	$L[\text{H}_2\text{S}(3)]$ ($10^{39} \text{ erg s}^{-1}$)	$L[\text{H}_2\text{S}(5)]$ ($10^{39} \text{ erg s}^{-1}$)	$L[\text{H}_2\text{S}(6)]$ ($10^{39} \text{ erg s}^{-1}$)	$L[\text{H}_2\text{S}(7)]$ ($10^{39} \text{ erg s}^{-1}$)
4935168	28.9 ± 11.89	14.59 ± 2.51	5.16 ± 2.57	5.34 ± 0.47	< 8.9	< 7.88	< 10.08
6650880	< 2419.43	544.47 ± 222.07	< 677.1	231.52 ± 84.55	304.17 ± 347.44	< 1083.2	< 885.41
22115072	< 290.4	295.51 ± 131.33	43.48 ± 25.74	91.32 ± 22.97	93.95 ± 67.61	< 224.95	< 178.68
4671744	< 0.09	0.28 ± 0.04	0.09 ± 0.03	0.38 ± 0.03	1.03 ± 0.07	< 0.28	0.19 ± 0.09
4985600	102.43 ± 41.22	908.96 ± 26.26	300.52 ± 21.8	513.38 ± 13.3	1192.94 ± 41.3	456.98 ± 36.12	203.6 ± 29.01
22079488	< 1.55	4.1 ± 0.63	1.57 ± 0.38	3.27 ± 0.47	6.69 ± 1.24	< 5.44	< 4.75
18526208	0.18 ± 0.03	1.91 ± 0.07	0.18 ± 0.04	0.3 ± 0.05	0.11 ± 0.09	0.12 ± 0.08	< 0.33
25408512	< 28.63	72.57 ± 11.67	17.14 ± 6.72	25.09 ± 6.83	< 53.85	< 42.81	< 40.28
20316160	49.4 ± 11.62	107.34 ± 10.61	< 14.19	25.29 ± 3.54	33.01 ± 13.36	< 54.89	< 34.9
22087680	< 0.32	0.33 ± 0.12	0.21 ± 0.08	0.76 ± 0.1	< 0.88	< 0.76	< 0.9

Table 3. Example PAH Results: We list the AORkey, the EQW[PAH 6.2 μm] (and upper limits in the case of $< 2\sigma$ $L[\text{PAH } 6.2 \mu\text{m}]$ detection), the PAH 6.2 μm PAH 7.7 μm and PAH 11.3 μm line luminosities in units of $10^{41} \text{ erg s}^{-1}$ with their respective errors for $\geq 2\sigma$ detections of 10 example objects or upper limits for $< 2\sigma$, and silicate feature strength $\tau_{9.7 \mu\text{m}}$. The full version of this table is available in on-line format.

AORkey	EQW[PAH 6.2 μm] (μm)	$L[\text{PAH } 6.2 \mu\text{m}]$ ($10^{41} \text{ erg s}^{-1}$)	$L[\text{PAH } 7.7 \mu\text{m}]$ ($10^{41} \text{ erg s}^{-1}$)	$L[\text{PAH } 11.3 \mu\text{m}]$ ($10^{41} \text{ erg s}^{-1}$)	$\tau_{9.7 \mu\text{m}}$
4935168	< 0.24	< 0.83	48.50 ± 5.40	1.18 ± 0.026	3.10
6650880	0.61	189.64 ± 7.94	841.37 ± 54.84	114.34 ± 5.31	1.88
22115072	1.5	72.21 ± 1.89	317.58 ± 3.70	48.32 ± 1.01	0.65
4671744	0.05	0.014 ± 0.002	0.018 ± 0.007	0.034 ± 0.001	0.25
4985600	0.51	57.52 ± 0.91	273.98 ± 15.61	57.18 ± 0.58	1.78
22079488	< 0.11	< 0.43	0.50 ± 0.08	0.35 ± 0.01	0.30
18526208	0.03	0.0092 ± 0.0021	0.0049 ± 0.0039	0.0175 ± 0.0012	−0.10
25408512	0.05	0.65 ± 0.34	3.14 ± 0.58	1.39 ± 0.21	0.57
20316160	1.99	51.26 ± 0.40	125.66 ± 4.29	27.51 ± 0.21	0.91
22087680	0.05	0.026 ± 0.006	0.084 ± 0.011	0.084 ± 0.002	0.20

We calculate the synthetic $W3$ and $W4$ magnitudes from our IRS spectra to test the flux calibration of the reduced IRS spectra and to test our spectral order scaling factors. We expect the offset between the synthetic and observed magnitudes to be within random error of the magnitude measurements if the spectra are correctly calibrated and stitched. We calculate the synthetic flux using

$$f_{\nu, \text{synth}} = \frac{\int f_{\nu}(\nu) S(\nu) d\nu}{\int S(\nu) d\nu}, \quad (1)$$

where $f_{\nu, \text{synth}}$ is the measured flux density averaged over the filter

profile, $f_{\nu}(\nu)$ is the calibrated flux density, and $S(\nu)$ is the filter's sensitivity response. We convert synthetic fluxes to Vega magnitudes using the zero points given in Jarrett et al. (2011). The median differences between the *WISE* synthetic and observed 12 and 22 μm bands are 0.11 and −0.10 mag respectively. We find these offsets do not significantly affect our analyses, and in the following paragraph we describe this as well as the fraction of objects in our sample that are most susceptible to the aperture differences between the *WISE* and IRS passbands. We show the offset between the observed and synthetic magnitude for the $W3$ and $W4$ bands in Figure 2.

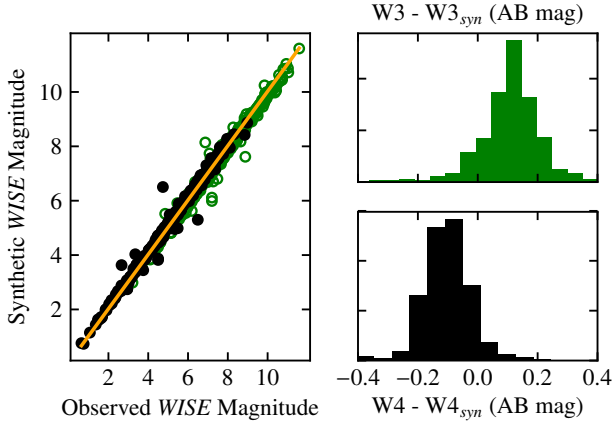


Figure 2. Spectrophotometry Test: In the leftmost plot, the filled black circles and the empty green circles are the 22 and 12 μm *WISE* bandpasses respectively. We calculate the synthetic *WISE* photometry by convolving the observed IRS spectrum with the relevant *WISE* bandpass transmission curve. We plot an orange line with a slope of one for visual reference. In the rightmost plots, we show the distribution of the difference of the observed to synthetic photometry for each band. The median differences between the *WISE* synthetic and observed 12 and 22 μm bands are 0.11 and -0.10 mag respectively.

We use the ratio of observed to synthetic *WISE* photometry to test for potential aperture biases. If an object is extended outside the IRS slit area, then the gas and dust measurements would be artificially smaller for that object. The aperture size of the *WISE* bandpass is 12 arcsec, implying that the ratio of observed to synthetic will increase if the object is extended in the SL module which has a width of 4.5 arcsec. Less than 10 per cent of our sample has 22 μm (*W4*) observed to synthetic ratios greater than 1.0, and our gas and dust relationships do not significantly change as a function of the ratio. We use the *W4* bandpass to calculate the synthetic magnitude at 24 μm via linear interpolation as follows:

$$f_v(24 \mu\text{m}) = f_v(22 \mu\text{m}) \left(\frac{24 \mu\text{m}}{22 \mu\text{m}} \right)^\alpha \quad (2)$$

where $f_v(22 \mu\text{m})$ is the *W4* band rest-frame synthetic flux and α is the spectral index calculated from the IRS spectroscopy between 15 and 30 microns.

We use the 24 μm photometry estimate to derive the 24 μm luminosities used throughout our analysis. We provide these luminosities in Table 1.

2.4 Redshifts

In Table 1 we provide the AORkeys, coordinates, redshift, and other general sample properties. The Infrared Database of Extragalactic Observables (IDEOS) has a redshift catalogue for all the spectra in CASSIS (Hernán-Caballero et al. 2016). The IDEOS redshift catalogue was compiled by comparing with the NASA/IPAC Extragalactic Database redshifts and optical counterparts, providing IRS redshifts with accuracy $\sigma_z \sim 0.0011$. Over 85 per cent of our initial sample of 2,807 objects have reliable redshift measurements, and we show the distribution of redshifts in Figure 3. The remaining objects have poor redshift determinations, so we exclude them from our sample. The median and mean redshifts for the objects in our sample with secure redshifts are 0.15 and 0.4 respectively.

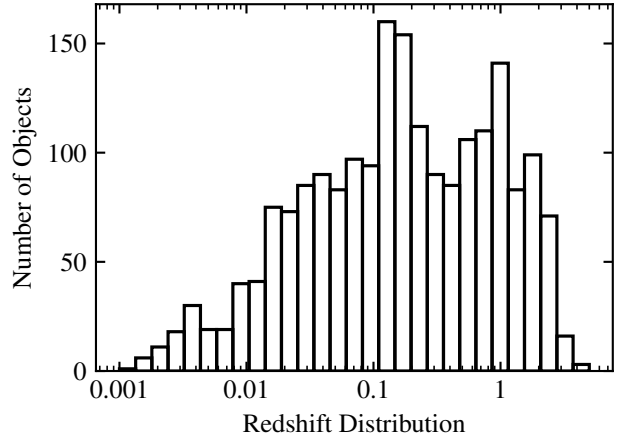


Figure 3. Redshift distribution from the cross-matched IDEOS objects. The median and mean redshifts for our sample are 0.15 and 0.4 respectively.

2.5 Emission Line Measurements

We measure the emission lines listed in Table 4. We denote the H_2 emission lines as $\text{H}_2\text{S}(J)$ for a transition from rotational level $J + 2$ to J . All of the H_2 features are unresolved, so the linewidths are set by the IRS spectral resolution and are listed in Smith et al. (2007). The line resolution changes after we apply a rest-frame correction. To account for this, we determine a fitting window by choosing only the points that are three Gaussian widths away relative to the linewidth of the feature. We allow the line centre of the feature in the rest-frame to vary 0.03 μm to take into account wavelength calibration uncertainty (Smith et al. 2007). We perform a linear least squares regression to find the best-fit parameters for our model, parametrized as

$$f_v(\lambda) = B + C(\lambda - \lambda_c) + D e^{-(\lambda - \lambda_c)^2 / 2\sigma^2}, \quad (3)$$

where B , C , D are the fitted constants, λ the wavelength array, λ_c the line centre, and σ the line resolution according to its wavelength location on the IRS spectrograph. We list the number of detections of each fitted line and their median signal-to-noise ratio in Table 4, and a subset of the values themselves in Table 2. We compare our molecular hydrogen measurements with Higdon et al. (2006) and Hill & Zakamska (2014), and find agreement within 0.2 dex.

2.6 Continuum and Dust Features

PAH molecules consist of planar lattices of aromatic rings containing tens to hundreds of carbon atoms. The absorption of UV photons excites their vibrational modes, which can contribute dramatically to the MIR emission. In stochastic dust grain heating models, the relative strengths of the PAH bands are dependent on the distribution of grain sizes and ionization states (Li & Draine 2001; Draine & Li 2007). The EQW[PAH 6.2 μm] feature probes the contribution of the AGN to the MIR spectrum. The PAH 6.2 μm feature appears to originate from SF hot dust (Peeters et al. 2004), and the 6 μm continuum is in a wavelength regime where the reprocessed light from the hot torus dominates. Therefore, the EQW[PAH 6.2 μm] should be some possibly non-linear function of the ratio of SF-sourced energy to AGN torus-sourced energy (Spoon et al. 2007). PAHs generate the broad emission features at 6.2, 7.7, and 11.3 μm (Allamandola et al. 1989), and these features

Table 4. Number of 2σ or greater detections and the median signal-to-noise ratio of the detections. Although we do not use the fine-structure lines in this paper, we provide our fluxes for ease of comparison to other published samples and analyses.

Line	Detection	Median SNR
[Ar II]6.985 μm	668	4.5
[Ar III]8.991 μm	220	3.4
[S IV]10.511 μm	585	4.4
[Ne II]12.81 μm	1135	8.9
[Ne III]15.56 μm	889	6.2
[S III]18.71 μm	609	5.6
[O IV]25.910 μm	520	7.3
[Fe II]25.989 μm	494	6.7
[S III]33.48 μm	395	5.7
H ₂ S(0)28.212 μm	73	2.7
H ₂ S(1)17.03 μm	585	7.0
H ₂ S(2)12.279 μm	159	4.0
H ₂ S(3)9.665 μm	512	5.8
H ₂ S(5)6.909 μm	244	2.7
H ₂ S(6)6.109 μm	70	7.5
H ₂ S(7)5.511 μm	82	4.8

contribute up to 30 per cent of the total MIR flux in galaxies whose star-formation processes dominate (Smith et al. 2007).

We model the PAH features using individual and blended Drude profiles (Smith et al. 2007; Hill & Zakamska 2014)

$$f_v^{(r)} = \frac{b_r \gamma_r^2}{(\lambda/\lambda_r - \lambda_r/\lambda)^2 + \gamma_r^2}, \quad (4)$$

where b_r is the fractional intensity, γ_r is the fractional FWHM, and λ_r the central wavelength. The integrated intensity of the Drude profile is

$$f^{(r)} = \int f_v^{(r)} dv = \frac{\pi c b_r \gamma_r}{2 \lambda_r}. \quad (5)$$

The rest-frame equivalent width of the Drude profile is

$$\text{EQW} = \frac{\pi}{2} \frac{b_r}{f_v^{\text{cont}}} \gamma_r, \quad (6)$$

where f_v^{cont} is the continuum flux density. We use the tabulated values for γ_r as presented in Smith et al. (2007). For the most AGN-dominated spectra (EQW[PAH 6.2 μm] < 0.01 μm), we find a non-negligible contribution from the [Ne VI] line which is blended with the 7.7 μm feature. We fit an additional Gaussian to account for this potential line. For the 6.2, 7.7, and 11.3 μm we have 2σ detections for 51, 58, and 56 per cent respectively for our sample. In Table 2 and Table 3, we show example H₂ and PAH fluxes for 10 objects. We used the results of Reyes et al. (2008) and Zakamska et al. (2008) extensively in training and refining our fitting procedures for both the emission line measurements and dust features.

PAHs trace the contribution of young B stars in PDRs (Peeters et al. 2004). The PAH 11.3 μm feature's continuum is easier to constrain than that of the 7.7 μm feature. As shown in Peeters et al.

Table 5. EQW[PAH 6.2 μm] mean per cent difference between the direct method/PAHFIT and the Drude profile method to estimate the fluxes and EQW of PAH emission features: For our stacked sample, the direct method yields slightly smaller equivalent widths than PAHFIT.

Method	EQW < 0.27 μm (AGN Dominated)	EQW > 0.27 μm (SF Dominated)
Drude – Direct	14%	52%
Drude – PAHFIT	–66%	20%

(2017a), and tested on a large sample of extragalactic IRS low-resolution observations in Stock & Peeters (2017), the full decomposition of the 7–9 μm PAH emission includes two components that are more similar to a dust continuum rather than to the 7.7 μm complex emission described in Li & Draine (2001). The emission of this dust continuum, referred to as a plateau, occurs in spatially distinct regions from the PAH emission, and overall behaves independently. Although there is also a 10–15 μm plateau, the emission in this region is less pronounced so that the 11.3 μm feature is only marginally affected. The 6.2 μm feature is in the wavelength regime where the AGN processes contribute to the continuum amplitude. Thus, we use the 11.3 μm feature to trace star-formation in our objects.

Other PAH measurement techniques widely used in the literature include: (1) direct integration of the feature super-imposed on a polynomial pseudo-continuum excluding other potentially contaminating lines or features (used in Brandl et al. 2006), and (2) simultaneous estimation of the contributions of PAHs, ions, molecules and old stellar populations to the observed spectra, e.g. PAHFIT (Smith & Draine 2012, used by Smith et al. 2007; O’Dowd et al. 2009; Shipley et al. 2013) and CAFE (Marshall et al. 2007, used by Stierwalt et al. 2014). We calculate the systematic offset between methods (1), (2), and our Drude measurements for our high signal-to-noise stacked spectra presented in subsection 2.7, and summarize the results in Table 5.

2.7 Spitzer Stacks

We stack a subset of our 2,015 *Spitzer* spectra in 100 equally populated bins of EQW[PAH 6.2 μm]. We only include objects with $z \leq 0.3$ to ensure the relevant features are not redshifted out of our wavelength range. After applying our z constraints, each bin contains 12 objects. After binning our sample by EQW[PAH 6.2 μm], we determine a weight for each individual spectrum given by its average signal-to-noise ratio in the region around the EQW[PAH 6.2 μm] feature. We assume the weight must be greater than or equal to 0.2, then normalize each spectrum by its rest-frame $L_{\nu}[24 \mu\text{m}]$ and perform a weighted average. We check that the width of the unresolved lines (the emission lines listed in Table 4) are equal to the *Spitzer* IRS minimum widths allowed by the instrument’s spectral resolution, and find that the widths vary negligibly from bin to bin. This is a check on the accuracy of our redshifts. The median absolute deviation of the spectra in each wavelength bin is less than 10 percent of each bin’s flux. We display these spectra, colour-coded by EQW[PAH 6.2 μm], in Figure 4.

We use the stacked spectra to identify and quantify differences between three methods to estimate the PAH emission. We use full spectral decomposition via PAHFIT, direct integration, and Drude model fitting. For the direct integration method we measure the associated continuum of the 6.2, 7.7, and 11.3 μm features by

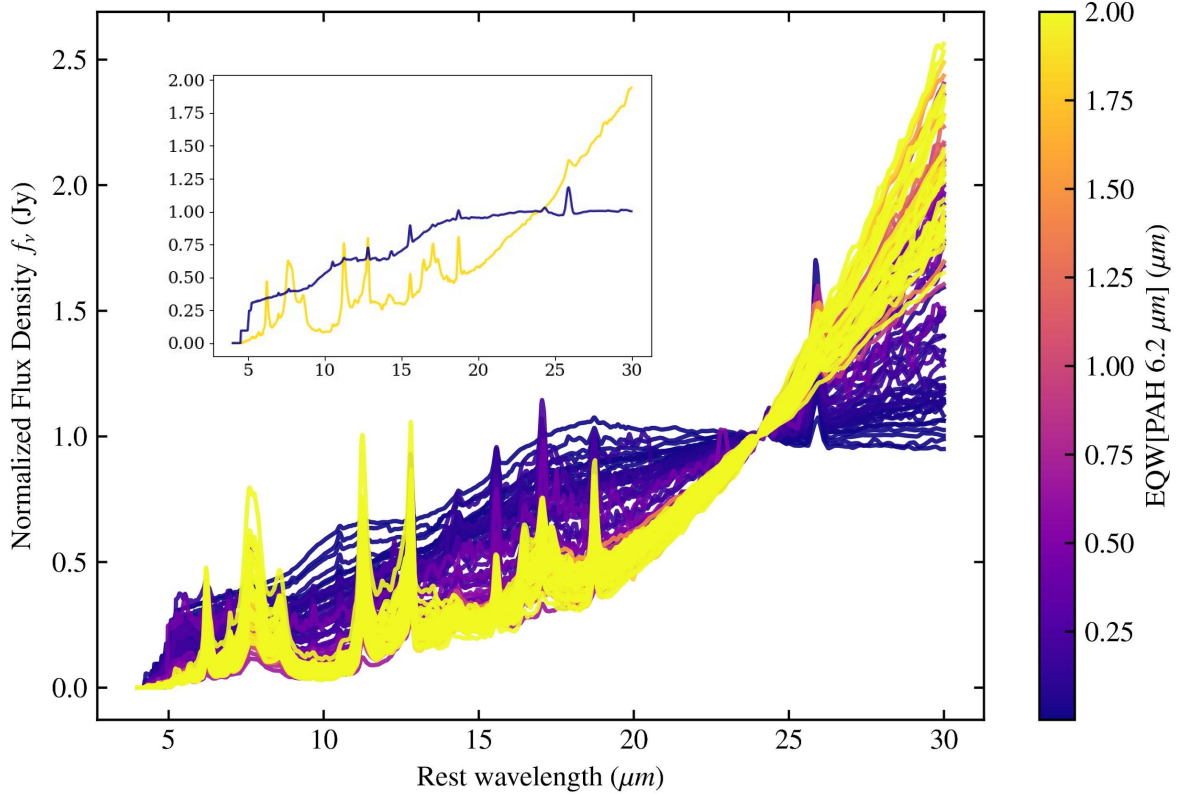


Figure 4. Stacked *Spitzer* spectra binned by EQW[PAH 6.2 μm]: we split our sample into 100 evenly populated bins of EQW[PAH 6.2 μm]. We normalize each pre-stacked individual spectrum by its IRS f_{ν} [24 μm]. We use the blue-to-yellow gradient colormap throughout this work to indicate the EQW[PAH 6.2 μm], with blue corresponding to AGN-dominated and yellow SF-dominated. The inset shows only two spectra from the stacks, a low EQW (blue) and high EQW (yellow) stack, and is meant to provide an easy comparison between the stacks. We provide the entirety of the stacked spectra in ASCII format in the on-line version of this publication.

performing a linear interpolation while excluding ice features and other emission lines that fall in the immediate vicinity of the PAH (Spoon et al. 2007). For the 6.2 μm feature we interpolate between 6.0 and 6.5 μm , for the 7.7 μm feature we interpolate between 7.3 and 8.3 μm , and for the 11.3 μm feature we interpolate between 11.0 and 11.8 μm . For PAHFIT, we input rest-frame calibrated (SL1–LL2 scale corrected, bonus order combined) spectra. We describe the Drude method in subsection 2.6.

We show the median and mean differences between the two methods and the Drude method in Table 5. We split the stacks into EQW[PAH 6.2 μm] < 0.27 μm and EQW[PAH 6.2 μm] > 0.27 μm . Since the ISO mission in the 1990s, the equivalent widths of PAHs have been used to separate AGN from SF dominated objects (Genzel et al. 1998). More recently, (Diamond-Stanic & Rieke 2010; Petric et al. 2011; Zakamska et al. 2016) verified the efficiency of this technique by comparing multiple MIR diagnostics including PAH EQW, MIR colours, and relative high to low ionization emission line fluxes. Here we continue with this approach, but we test the robustness of our measurement as a function of measurement method: assuming a Drude model (Draine 2003; Smith et al. 2007), direct integration (Brandl et al. 2006), and simultaneous estimation using PAHFIT (O’Dowd et al. 2009).

In Figure 4, the difference in the relative continuum emission in the 6.2 μm region is clear. In subsection 3.1, we show this region is a good differentiator between AGN versus SF dominated spectra via comparison to other MIR diagnostics. Thus it is important to test the consistency of the different PAH fitting algorithms on high signal to noise spectra with varying amounts of PAH emission. We test whether the algorithms agree for different AGN contributions to the MIR. We subtract the direct and PAHFIT measured EQW values from the Drude profile values and find the median and mean of the differences. The treatment of the continuum around the PAH emission feature accounts for most of the differences between PAH EQW estimates obtained from the three different methods. Direct methods tend to underestimate the continuum for the most SF-dominated spectra, unless one fits separately in the 7.7 and 11.3 μm regions the 5–10 and 10–15 μm plateaus (Peeters et al. 2017b). We choose the Drude method because it is less sensitive to potential poor quality pixel values (unlike the direct method) and estimates the continuum more consistently than PAHFIT.

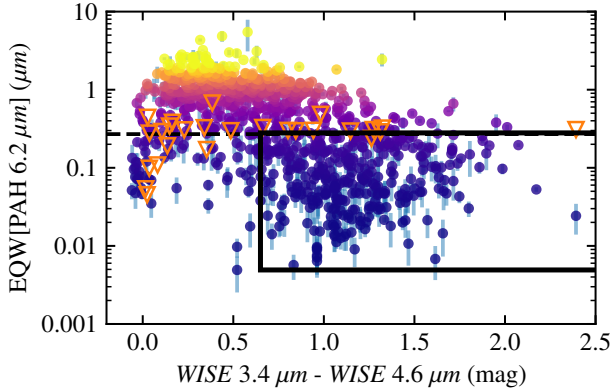


Figure 5. AGN selection comparison: Using a *WISE* colour cut that is dependent on the *W2* magnitude as outlined in [Assef et al. \(2013\)](#), we capture 80 per cent of our objects that satisfy the AGN criterion $\text{EQW}[\text{PAH } 6.2 \mu\text{m}] < 0.27 \mu\text{m}$. The solid black box encapsulates roughly all of the objects that satisfy both the EQW threshold and *WISE* colour cut. The dashed black line marks the EQW threshold of AGN MIR dominance at $0.27 \mu\text{m}$. The orange triangles are EQW[PAH $6.2 \mu\text{m}$] upper limits for objects with 2σ detections of $\text{H}_2\text{S}(3)$, PAH $7.7 \mu\text{m}$, and PAH $11.3 \mu\text{m}$. The colours of the points are the same as in previous figures, with blue denoting AGN-dominated objects and yellow denoting SF-dominated objects, defined by having small and large values of EQW[PAH $6.2 \mu\text{m}$] respectively.

3 RESULTS

3.1 The AGN contribution to the MIR emission

A significant fraction of MIR emission in AGN host galaxies comes from dust heated by $\lambda < 10 \mu\text{m}$ photons (e.g. [Nenkova et al. 2008](#)). We adopt the empirical thresholds of AGN contribution to the MIR presented in [Laurent et al. \(2000\)](#), [Peeters et al. \(2004\)](#), [Brandl et al. \(2006\)](#), and [Armus et al. \(2007a\)](#). If the EQW[PAH $6.2 \mu\text{m}$] is less than $0.27 \mu\text{m}$, the AGN contributes more than 50 per cent of the MIR emission and we refer to those sources as AGN-dominated. If the EQW[PAH $6.2 \mu\text{m}$] is larger than $0.27 \mu\text{m}$ but less than $0.54 \mu\text{m}$, we classify the spectrum as a composite object with signatures of both AGN and SF. If the EQW[PAH $6.2 \mu\text{m}$] is $> 0.54 \mu\text{m}$, then we classify the object as SF dominated. Subsection 2.7 visually demonstrates that the PAH $6.2 \mu\text{m}$ feature effectively differentiates between AGN and SF dominated MIR spectra: when we select AGN dominated targets on the basis of their EQW[PAH $6.2 \mu\text{m}$] we also find them to be AGN dominated on the basis of their continuum slopes between 15 to $30 \mu\text{m}$. Using the EQW[PAH $6.2 \mu\text{m}$] selection method we find: 40 per cent AGN dominated, 12 per cent composite, 48 per cent SF dominated.

Photometric observations in the MIR have been used to find AGN with *Spitzer* ([Lacy et al. 2004](#); [Stern et al. 2005](#); [Martínez-Sansigre et al. 2005](#); [Lacy et al. 2007](#); [Stern et al. 2005](#); [Donley et al. 2012](#); [Eisenhardt et al. 2012](#); [Lacy et al. 2015](#)) and *WISE* ([Stern et al. 2012](#); [Assef et al. 2013](#)). As with most selection methods, there is a trade-off between completeness and reliability (e.g. [Petric et al. 2011](#); [Assef et al. 2013](#)). We use [Assef et al. \(2018\)](#)'s *WISE* AGN selection criterion, which is 90 percent reliable and 17 per cent complete. We compare this criterion to the EQW[PAH $6.2 \mu\text{m}$] selection in [Figure 5](#). Of the 2,105 objects in our overall *Spitzer* sample, 52 per cent satisfy the colour criteria by [Assef et al. \(2018\)](#). Of the [Assef et al. \(2018\)](#) selected objects, 65 per cent are classified as AGN using

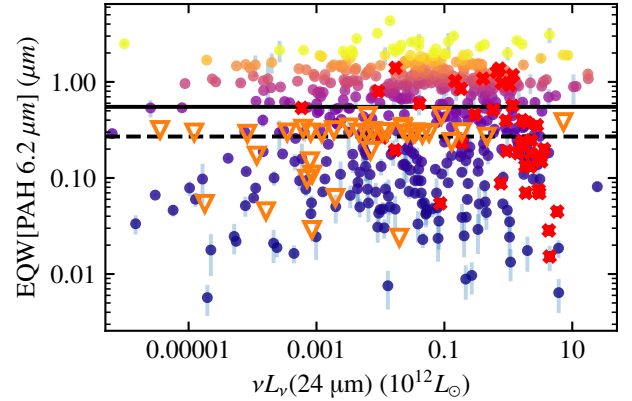


Figure 6. $24 \mu\text{m}$ luminosity selection: The solid black horizontal line is the mean EQW of normal star-forming galaxies as described in [Brandl et al. \(2006\)](#). The dashed black horizontal line is the empirical AGN dominance EQW classifier. We find that although the majority of objects with large $24 \mu\text{m}$ luminosities have small $6.2 \mu\text{m}$ equivalent widths, most do not follow this trend; 80 per cent of our targets have low EQW[PAH $6.2 \mu\text{m}$] and $24 \mu\text{m}$ luminosities $< 10^{11} L_{\odot}$. Bold red crosses show the 70 objects that follow the trend found by [Desai et al. \(2007\)](#) for ULIRGs. The orange triangles are EQW[PAH $6.2 \mu\text{m}$] upper limits for objects with $< 2\sigma$ detections of $\text{H}_2\text{S}(3)$, PAH $7.7 \mu\text{m}$ and PAH $11.3 \mu\text{m}$. The colours of the points are the same as in previous figures, with blue denoting AGN-dominated objects and yellow denoting SF-dominated objects, defined by having small and large values of EQW[PAH $6.2 \mu\text{m}$] respectively.

EQW[PAH $6.2 \mu\text{m}$]. Conversely, of the 2,105 objects in the overall sample that satisfy the EQW[PAH $6.2 \mu\text{m}$] criterion, 80 per cent are selected. The EQW[PAH $6.2 \mu\text{m}$] criterion is calibrated to rule out SF–AGN composites. Selecting with a less stringent threshold, $\text{EQW}[\text{PAH } 6.2 \mu\text{m}] < 0.54 \mu\text{m}$ (i.e. AGN-dominated and SF–AGN composites), we get 52.4 per cent of our total sample classified as AGN, and are in good agreement with the [Assef et al. \(2018\)](#) selection in the MIR colour selected sub-sample. Although this fraction is not impressively high, it is in qualitative agreement with other studies that demonstrate that spectroscopically-selected AGN are recovered by color selection methods at roughly the same rate ([Yuan et al. 2016](#)).

The completeness of a selection method can depend on the AGN type. Using the *WISE* colour wedge as defined in [Mateos et al. \(2012\)](#) on a sample of Type 2 quasars, [Yuan et al. \(2016\)](#) find that only 34 per cent of these fit the [Mateos et al. \(2012\)](#) AGN selection criterion, which is 90 percent reliable and 17 percent complete. In [Figure 5](#), there is a grouping of 26 objects with small equivalent widths but with *WISE* colours that suggest they are star-forming ($\text{EQW}[\text{PAH } 6.2 \mu\text{m}] < 0.27 \mu\text{m}$ and $W1 - W2 < 0.1$). We perform a literature search with the coordinates of these 26 objects, and find that 10 are FRI radio galaxies from the 3C sample ([Ogle et al. 2010](#)). [Gürkan et al. \(2014\)](#) found that *WISE* colour wedges tend to miss these low-luminosity radio galaxies. Furthermore, [Blecha et al. \(2018\)](#) find that *WISE* colour-cuts that are too stringent (i.e. $W1 - W2 > 0.8$) can miss AGN in late stage mergers. As seen in [Figure 5](#), 10 per cent of low EQW[PAH $6.2 \mu\text{m}$] objects would be missed with the above colour-cut. Due to its consistency with different AGN host-galaxy classes, this justifies our use of EQW[PAH $6.2 \mu\text{m}$] as AGN-dominated spectra selection criterion.

Monochromatic continuum luminosity at $24 \mu\text{m}$ is commonly used to trace star-formation due to the warm dust associated with

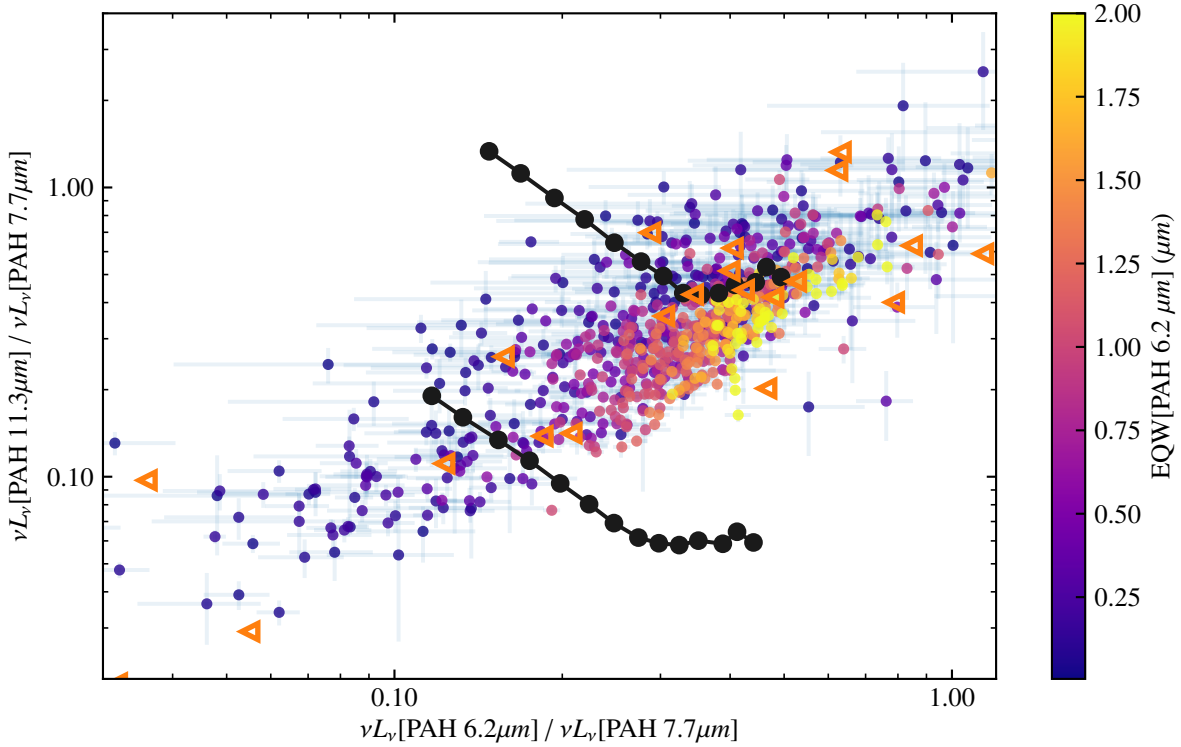


Figure 7. PAH band ratios: The black lines correspond to the expected ratios for fully neutral (top) or fully ionized (bottom) PAH molecules of a given number of carbon atoms using [Draine & Li \(2007\)](#) models. The orange triangles are EQW[PAH 6.2 μm] upper limits for objects with $< 2\sigma$ detections of H₂S(3), PAH 7.7 μm and PAH 11.3 μm . The colours of the points are the same as in previous figures, with blue denoting AGN-dominated objects and yellow denoting SF-dominated objects, defined by having small and large values of EQW[PAH 6.2 μm] respectively.

high-mass star-forming regions ([Calzetti et al. 2007](#)). [Desai et al. \(2007\)](#) and others find a linear trend between EQW[PAH 6.2 μm] and 24 μm luminosity for the most luminous $z < 1.0$ ULIRGs, suggesting that at these redshifts, only galaxies with AGN contain large amounts of warm dust. In our sample, we find that although the majority of objects with large 24 μm luminosities have small EQW[PAH 6.2 μm], objects with small EQW[PAH 6.2 μm] have diverse 24 μm luminosities. The 24 μm luminosities for these objects are indistinguishable from objects with larger values of EQW[PAH 6.2 μm]. [Figure 6](#) shows that in our sample, we cannot identify the contribution of the AGN to the total MIR emission using only the 24 μm luminosities. As noted in [Desai et al. \(2007\)](#), despite their correlation between EQW[PAH 6.2 μm] and 24 μm luminosity for local ULIRGs, sub-millimetre galaxies can have high EQW[PAH 6.2 μm] and high 24 μm luminosities. Furthermore, [Petric et al. \(2011\)](#) find no correlation amongst LIRGs ($L_{\text{IR}} < 10^{11} L_{\odot}$). The tight correlation observed in ULIRGs between 24 μm luminosities and EQW[PAH 6.2 μm] can be explained by the compact IR emission in ULIRGs and the relative high fraction of AGN dominated ULIRGs (40–60 per cent). ULIRGs also tend to be in the final stages of merging, while LIRGs span all stages of gravitational interactions. While a census of the merging stages in our sample is beyond the scope of this paper, we speculate that the galaxies in our sample have a wide range of morphologies and merger stages. Thus, it is not surprising that we do not find a relationship in our sample of mixed infrared luminosities and galaxy sub-classes.

[Laurent et al. \(2000\)](#) combine both continuum emission and PAH EQW to estimate AGN contribution to the total IR. In [Fig-](#)

[ure 8](#), we use the revised version of the [Laurent et al. \(2000\)](#) selection method presented in [Armus et al. \(2007b\)](#) which uses the relative flux of the 6.2 μm PAH complex and 15 μm continuum versus the 5.5 μm continuum. Our method agrees with [Laurent et al. \(2000\)](#)'s: 98 per cent of the objects that the [Laurent et al. \(2000\)](#) criterion select as having 50 per cent or more AGN contribution have EQW[PAH 6.2 μm] $< 0.27 \mu\text{m}$. Although the main purpose of this figure is to compare the EQW[PAH 6.2 μm] selection to a common MIR AGN selection method, we also test if the correlation found in [Laurent et al. \(2000\)](#) and [Armus et al. \(2007b\)](#) is driven by the shared dependence of both variables, $f_{\nu}[6.2 \mu\text{m}]/f_{\nu}[5.5 \mu\text{m}]$ and $f_{\nu}[15 \mu\text{m}]/f_{\nu}[5.5 \mu\text{m}]$, on the 5.5 μm flux. We perform a partial correlation analysis parametrized as:

$$r_{12,3} = \frac{r_{12} - r_{13}r_{23}}{\sqrt{1 - r_{13}^2}\sqrt{1 - r_{23}^2}} \quad (7)$$

where the indices 1,2,3 refer to $f_{\nu}[6.2 \mu\text{m}]/f_{\nu}[5.5 \mu\text{m}]$, $f_{\nu}[15 \mu\text{m}]/f_{\nu}[5.5 \mu\text{m}]$, and $f_{\nu}[5.5 \mu\text{m}]$ respectively. The correlation coefficients are the Spearman Rank correlation coefficients. We find the correlation is not dominated by the shared $f_{\nu}[5.5 \mu\text{m}]$ values.

As discussed in previous papers (e.g. [Petric et al. 2011](#)), low resolution spectra cannot be used to deblend the [Cl II]–[Ne v] 14.322 μm lines. Furthermore, some AGNs do not show coronal line emission (e.g. Mrk 231: [Armus et al. 2007a](#)). After comparing multiple MIR AGN dominance criteria on our sample of low-resolution spectra, we use the EQW[PAH 6.2 μm] criterion to select MIR AGN dominated host galaxies.

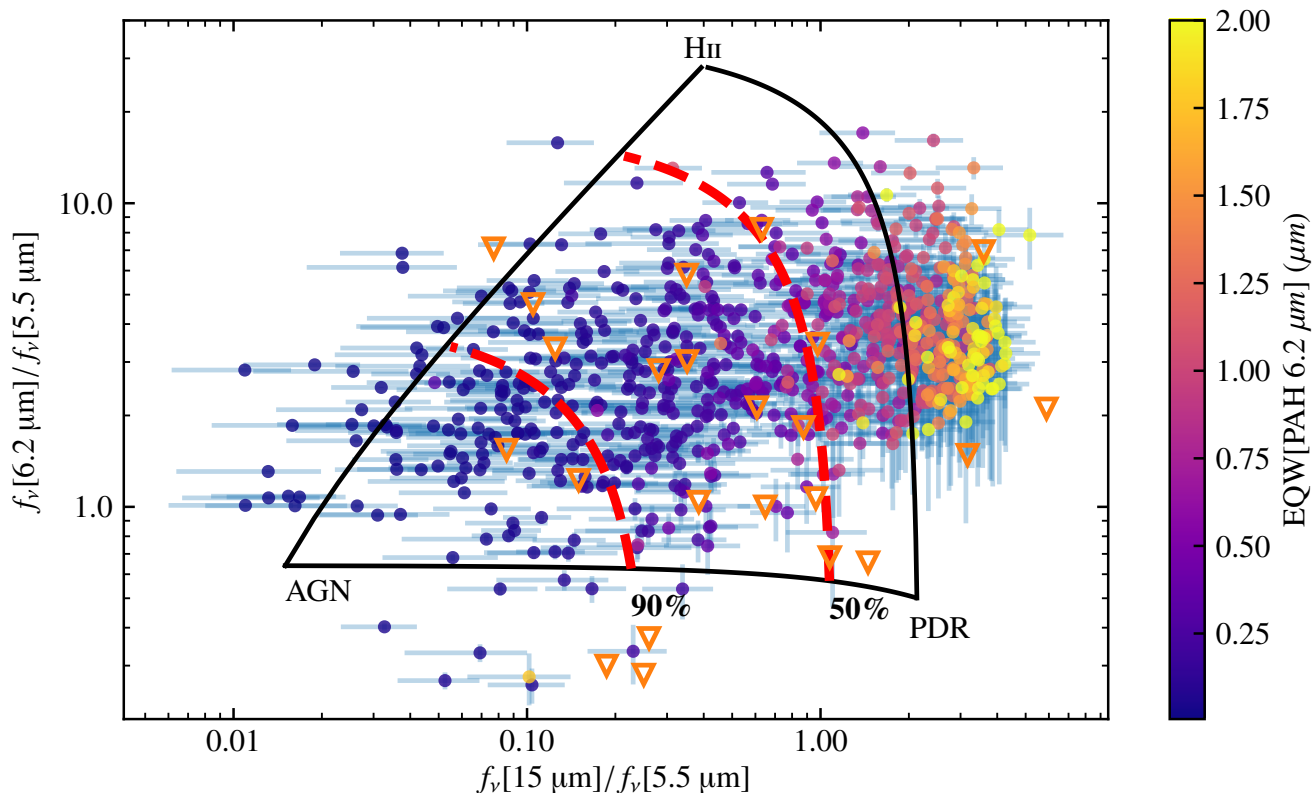


Figure 8. AGN selection comparison: The three vertices of the triangle are published values of an independently classified AGN (3C 273, [Weedman et al. 2005](#)), PDR (M17, [Peeters et al. 2004](#)) and H II region (NGC 7023, [Peeters et al. 2004](#)). The red-dashed lines represent (left) 90 per cent and (right) 50 per cent AGN contribution to the MIR. The diagram compares the integrated continuum flux from 14–16 μm denoted $f_{\nu}(15 \mu\text{m})$ to the integrated continuum flux from 5.3–5.8 μm denoted $f_{\nu}(5.5 \mu\text{m})$. The $f_{\nu}(6.2 \mu\text{m})$ values were derived as described in [subsection 2.6](#). The orange triangles are EQW[PAH 6.2 μm] upper limits for objects with $< 2\sigma$ detections of H₂S(3), PAH 7.7 μm , and PAH 11.3 μm . The colours of the points are the same as in previous figures, with blue denoting AGN-dominated objects and yellow denoting SF-dominated objects, defined by having small and large values of EQW[PAH 6.2 μm] respectively.

3.2 PAH Emission Features

We estimate the ionization state and grain size distribution from the relative strengths of PAH emission features. The emission of the 6.2 and 7.7 μm bands are attributed to the radiative relaxation of the carbon-carbon stretching mode, which is more common in ionized PAH molecules ([Tielens 2005](#)). The 11.3 μm feature emission, from carbon-hydrogen modes, drops by an order of magnitude between completely neutral and completely ionized PAH clouds. The ratio between the 6.2 and 7.7 μm features should not vary significantly as the ionization fraction changes ([Li & Draine 2001](#); [Draine & Li 2007](#)). The relative power emitted in a PAH band depends on the distribution of grain sizes because smaller dust grains radiate more at shorter wavelengths ([Li & Draine 2001](#); [Draine & Li 2007](#)).

We compare our estimates of $L[6.2 \mu\text{m}]/L[7.7 \mu\text{m}]$ and $L[11.3 \mu\text{m}]/L[7.7 \mu\text{m}]$ with theoretical values for completely ionized and completely neutral dust grains from [Draine & Li \(2007\)](#). [Figure 7](#) shows that sources with EQW[PAH 6.2 μm] $< 0.27 \mu\text{m}$, i.e. AGN dominated galaxies, have a wider range of relative strengths and 20 per cent have ratios below the theoretical line of ionization. The [Draine & Li \(2007\)](#) models were calculated using a single Milky Way-based model, and PAH band-strengths have been found above and below the model limits ([Diamond-Stanic & Rieke 2010](#); [Haan et al. 2011](#)). In addition, different PAH fitting methods can lead to different PAH band ratios ([O’Dowd et al. 2009](#)).

Thus, we do not feel justified to speculate on the possible physical processes that led to the PAH flux ratios we measure below the theoretical limits for fully ionized PAH. As seen in normal galaxies and LIRGs, non-AGN form a tight locus ([O’Dowd et al. 2009](#); [Shipley et al. 2013](#); [Stierwalt et al. 2014](#)). In [Figure 9](#), we calculate PAH ratios for our stacked spectra and find similar ranges of PAH relative strengths.

3.3 Warm Molecular Gas and Dust Luminosity Relationships

In galaxies where star-formation processes dominate the IR emission, H₂ and PAH emission are tightly correlated with an average value of H₂/PAH = 0.0065 ± 0.001 ([Roussel et al. 2007](#)). This suggests that the bulk of H₂ and PAH emission comes from gas and dust heated by similar sources. If star-forming regions emit a relatively constant amount of H₂ relative to PAH emission, and if PAH EQW decreases in regions where the AGN contributes to the IR emission, then we expect higher ratios of H₂ to PAH emission in sources with AGN. If the AGN heats the surrounding host material, then we may expect an additional warmer H₂ component associated with the AGN.

We find an anti-correlation between EQW[PAH 6.2 μm] and H₂ to PAH ratio. We estimate the ratios of H₂ to PAH emission

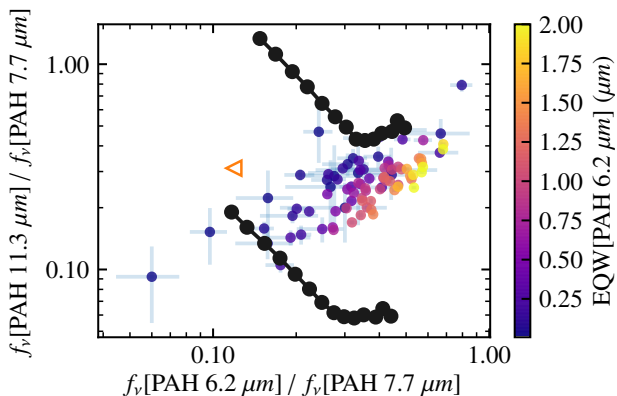


Figure 9. Stacked Spectra PAH band ratios: We show the normalized PAH relative strength ratios for our stacked spectra. Even in these high SNR spectra, there are AGN dominated sources below the theoretical line of complete ionization (bottom black line), and above the theoretical line of complete neutrality (top black line) (Draine & Li 2007). The open orange triangle is relative strength ratio calculated via a stack of the objects with only PAH 6.2 μm upper limits, but with 2σ detections of H₂S(3), PAH 11.3 μm , and PAH 7.7 μm . The colours of the points are the same as in previous figures, with blue denoting AGN-dominated objects and yellow denoting SF-dominated objects, defined by having small and large values of EQW[PAH 6.2 μm] respectively.

for all sources in our sample with 2σ detections of H₂S(3), PAH 11.3 μm , and PAH 6.2 μm . The 11.3 μm feature is often used to estimate star-formation rates (Peeters et al. 2004; Calzetti et al. 2007; Diamond-Stanic & Rieke 2010). Zakamska et al. (2016) find that PAH emission may be suppressed in quasars. With a sample of lower-luminosity AGN, Jensen et al. (2017) caution against using a simple relation between the 11.3 μm PAH flux and star-formation rates, though at large scales the method is reasonably reliable. We corroborate the PAH 11.3 μm flux invariance for lower-luminosity AGN on the large scales probed by the IRS spectrograph by finding a statistically significant weak correlation between EQW[PAH 6.2 μm] and PAH 11.3 μm luminosity for a $\geq 2\sigma$ PAH detected sub-sample comprised of 108 and 308 AGN and SF galaxies respectively (r_s : 0.15, $p_s < 0.003$). To estimate what fraction of the observed H₂ emission comes from gas in photo-dissociation regions, we divide the H₂S(3) 9.665 μm transition flux by the PAH 11.3 μm flux.

In Figure 10 we infer a large range of H₂ to PAH ratios (0.005–1.42). For EQW[PAH 6.2 μm] > 0.54 μm , our values are consistent with the H₂ to PAH ratios found in normal galaxies and SF dominated U/LIRGs (Rigopoulou et al. 2002; Roussel et al. 2007; Zakamska 2010; Stierwalt et al. 2014). In Figure 10, we show the expected strong inverse correlation between SF (via increasing EQW[PAH 6.2 μm]) and H₂ to PAH ratio (via increasing $L[\text{H}_2\text{S}(3)]/L[\text{PAH } 11.3 \mu\text{m}]$). We plot the theoretically calculated upper limit presented in Stierwalt et al. (2014) of the H₂ to PAH ratio, assuming all the H₂ is being fluorescently excited in PDRs (Le Petit et al. 2006).

There is a statistically significant correlation between the EQW[PAH 6.2 μm] and H₂ to PAH ratio. Assuming the $L[\text{H}_2\text{S}(3)]$ normalized by $L[\text{PAH } 11.3 \mu\text{m}]$ accounts for the H₂ emission due to SF processes and EQW[PAH 6.2 μm] traces the hot dust emission directly related to the power of the AGN, the anti-correlation between the EQW[PAH 6.2 μm] and H₂ to PAH ratio suggests that the luminosity of H₂ scales with AGN activity (r_s : -0.6,

$p_s \ll 0.001$). The median $L[\text{H}_2\text{S}(3)]/L[\text{PAH } 11.3 \mu\text{m}]$ is 0.17 for AGN-dominated objects and 0.06 for SF-dominated objects. We use a two-sample KS test to quantify the differences between the H₂ to PAH ratio distributions of AGN and of star-formation dominated galaxies, and find that the distributions are different. We also find that the PAH 11.3 μm emission is not correlated with the EQW[PAH 6.2 μm] (r_s : 0.17, $p_s \ll 0.001$), and thus our EQW[PAH 6.2 μm] and H₂ to PAH ratio is not due to the differences of the PAH 11.3 μm emission between AGN and SF dominated galaxies. We perform a partial correlation analysis with the parametrization defined in 7, and find the shared dependency on PAH fluxes is not driving the correlation.

We test whether our results are redshift dependent by splitting the 2σ H₂ and PAH detections into equal bins of redshift space. We find the distribution of H₂ to PAH does not change within each bin. We perform a two-sample KS test, and find that the distributions in each bin are statistically indistinguishable from one another.

In ULIRGs, there is no evidence for extinction affecting molecular hydrogen emission (Higdon et al. 2006; Zakamska 2010). We test whether our sample is affected by extinction. We approximate the amount of extinction as proportional to the strength of the 9.7 μm silicate feature, a Si–O stretching resonance at 9.7 μm . We measure the strength of the 9.7 μm silicate absorption (or emission) feature given by

$$\tau_{9.7 \mu\text{m}} \equiv -\ln\left(\frac{f_{v,\text{obs}}[9.7 \mu\text{m}]}{f_{v,\text{cont}}[9.7 \mu\text{m}]}\right), \quad (8)$$

where $f_{v,\text{obs}}[9.7 \mu\text{m}]$ is the observed flux at 9.7 μm and $f_{v,\text{cont}}[9.7 \mu\text{m}]$ is the inferred continuum (Spoon et al. 2007; Zakamska 2010). We provide the silicate strengths in Table 3.

Figure 11 shows that there is no statistically significant trend between $\tau_{9.7 \mu\text{m}}$ and the ratio of the H₂S(3) and H₂S(1) transitions. Obscuration affects the measured PAH flux ratios. We plot each relative strength as a function of the silicate strengths in Figure 12. As seen in Zakamska (2010), the relationship found for $L[\text{PAH}[11.3 \mu\text{m}]]/L[\text{PAH}[7.7 \mu\text{m}]]$ indicates similar effects for both SF and AGN dominated galaxies (r_s : -0.76, $p_s \ll 0.001$, -0.72, $p_s \ll 0.001$, for AGN, SF dominated objects respectively). For $L[\text{PAH}[6.2 \mu\text{m}]]/L[\text{PAH}[7.7 \mu\text{m}]]$, we find the most SF dominated objects are located in a tight locus, and exhibit a much weaker correlation (r_s : -0.19, $p_s = 0.07$) than the rest of the sample. Zakamska (2010) explain the obscuration effects as evidence of PAHs existing behind the location of silicates and water ices in AGN dominated galaxies.

3.4 Warm and Warmer Molecular Hydrogen Temperature Decomposition

We investigate if the distributions of H₂ excitation temperatures we measure in AGN hosts differ from those of non-AGN galaxies. We estimate the typical temperatures of H₂ in SF-dominated and AGN-dominated galaxies using two different approaches: (1) Two Temperature Distributions – using all of the H₂ lines simultaneously to separate two different H₂ gas distributions within a given galaxy and (2) – Excitation Temperatures per Line Pair – excitation temperatures of H₂ transitions of equal parity without assuming multiple temperature distributions. Both (1) and (2) are the most standard ways of extricating the physical properties of the warm H₂ gas in astrophysical sources. Within (1) and (2) we explore two different methods for each approach: (1A, 2B) represent the most common implementation in the literature and (1B, 2B) represent new algorithms we have developed for these approaches using Bayesian

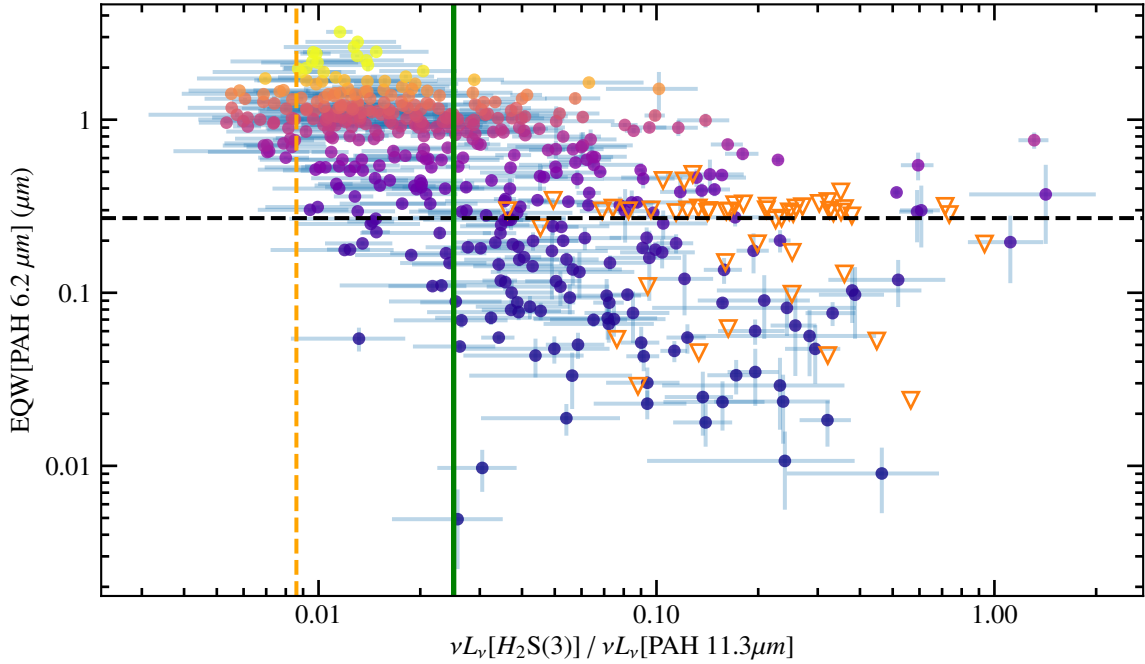


Figure 10. AGN activity versus molecular hydrogen excess emission: 2σ detections of the EQW[PAH 6.2 μm], $L(\text{H}_2\text{S}(3))$ and $L(\text{PAH}[11.3 \mu\text{m}])$ emission features. The black dashed horizontal line represents the EQW[PAH 6.2 μm] threshold (< 0.27) to signify AGN dominance. The dashed orange vertical line is the mean H_2 –PAH ratio from the SINGS normal star-forming galaxies sample (Roussel et al. 2007). The vertical green line is the upper limit of the H_2 to PAH ratio that is consistent with PDR emission as calculated via the Meudon PDR models (Le Petit et al. 2006) and presented in Stierwalt et al. (2014). The orange, open downward triangles are EQW[PAH 6.2 μm] upper limits. The value of the correlation is $r_s: -0.6$ with $p_s \ll 0.001$. The orange triangles are EQW[PAH 6.2 μm] upper limits for objects with $< 2\sigma$ detections of $\text{H}_2\text{S}(3)$, PAH 7.7 μm , and PAH 11.3 μm . The colours of the points are the same as in previous figures, with blue denoting AGN-dominated objects and yellow denoting SF-dominated objects, defined by having small and large values of EQW[PAH 6.2 μm] respectively.

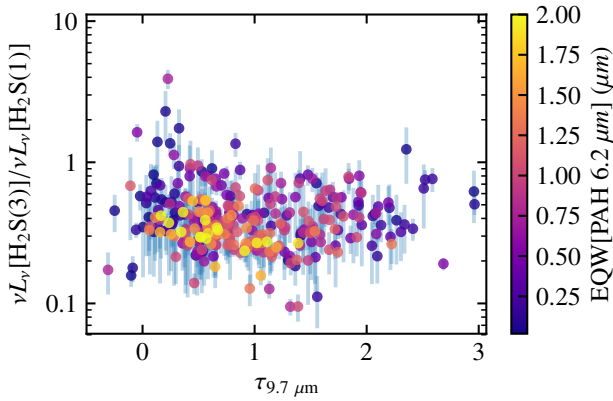


Figure 11. Molecular hydrogen emission versus silicate strength: H_2 emission is not significantly affected by extinction. We calculate the apparent silicate strength and compare it to the ratio $\nu L_\nu[\text{H}_2\text{S}(3)]/\nu L_\nu[\text{H}_2\text{S}(1)]$ (r_s , p -value is greater than 0.01, giving no evidence to discount the null hypothesis of no correlation). The colours of the points are the same as in previous figures, with blue denoting AGN-dominated objects and yellow denoting SF-dominated objects, defined by having small and large values of EQW[PAH 6.2 μm] respectively.

statistics. We use multiple methods to estimate H_2 excitation temperatures to test if our conclusions about the warm H_2 gas are ro-

Table 6. Summary of Warm H_2 Temperature Analysis Algorithms

Approach	Method A	Method B
(1) - Two Temperature Decomposition	Least-Squares Line Fitting to the Excitation Diagrams	Marginalized Likelihood Analysis
(2) - Excitation Temperatures	Means of the temperatures in a given transition	Hierarchical Bayesian Model

bust. We summarize the names and descriptions of our techniques in Table 6.

Two Temperature Decomposition: For (1), the two-temperature decomposition, we aim to decompose the H_2 excitation diagrams of the galaxies in our sample into two distributions: a warm and a warmer component. In both the unstacked and stacked spectra, the rotational transition ladders of the few galaxies in the dataset with high-significance detections of the $\text{H}_2\text{S}(0)$ through $\text{H}_2\text{S}(3)$ and $\text{H}_2\text{S}(5)$ through $\text{H}_2\text{S}(7)$ transitions cannot be described by a single excitation temperature; the higher-excitation H_2 transitions tend to be at higher temperatures than the lower-excitation transitions. In some of these well-detected rotational transition ladders, one can see the saw-tooth pattern characteristic of a non-equilibrium ortho-to-para ratio (Neufeld et al. 2006; Ogle et al. 2010). This motivates the two-temperature

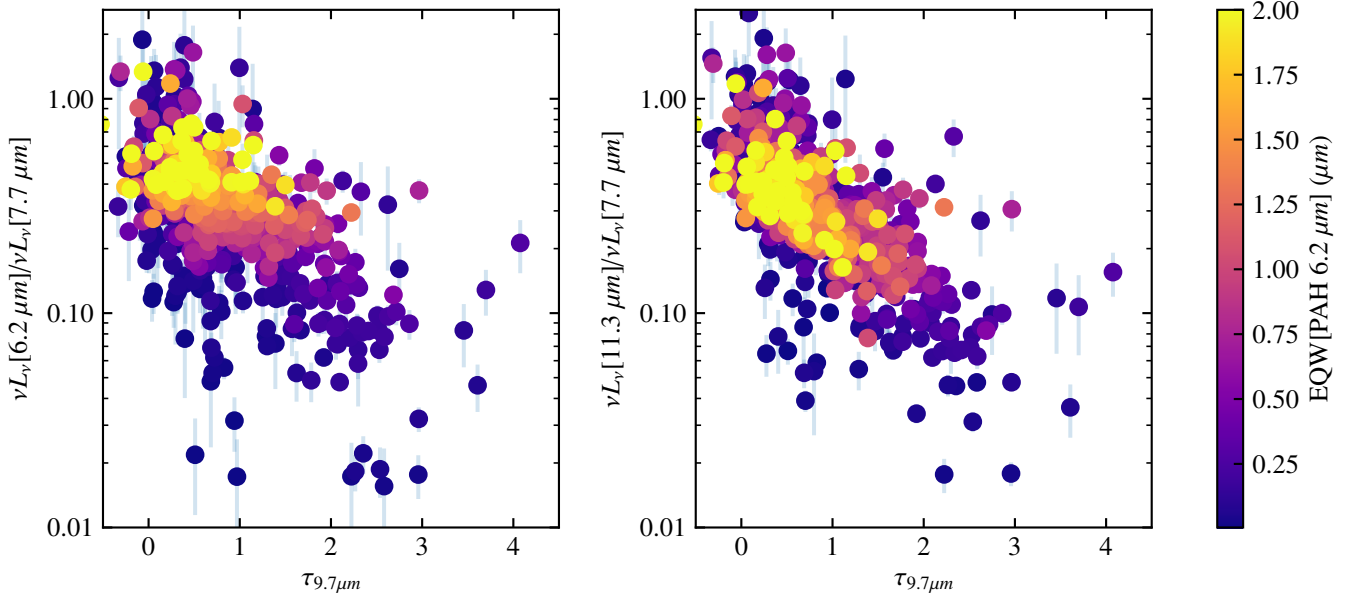


Figure 12. PAH band ratios versus silicate strength: We test how the diversity of PAH relative strengths relates to silicate obscuration. We use the 9.7 μm feature as tracer of obscuration. The orange triangles are EQW[PAH 6.2 μm] upper limits for objects with $< 2\sigma$ detections of $\text{H}_2\text{S}(3)$, PAH 7.7 μm and PAH 11.3 μm . The points are colour-coded by absorption strength, i.e. the red points have the greatest absorption, and the blue points the greatest emission. Light green points represent objects without significant silicate absorption or emission.

decomposition approach for modelling the excitation diagram with one warm component at 100 K – 300 K and another warmer component at > 300 K. Unfortunately, if we were to require 2σ detections of all lines at once, we would have fewer than 50 objects. Warm molecular hydrogen studies usually include upper limits for the non-significant detections in order to estimate the underlying temperature distribution. By analysing all of the H_2 lines simultaneously, we are able to provide a mass estimate of the H_2 in a given distribution. For (1A), we use the two-temperature decomposition algorithm as outlined in Higdon et al. (2006). This method and its variants are the most common techniques for extricating the warm and warmer components of the H_2 gas (Roussel et al. 2007; Ogle et al. 2010; Petric et al. 2018).

As Roussel et al. (2007), Higdon et al. (2006), and Petric et al. (2018) find, the mass can be severely biased if the $\text{H}_2\text{S}(0)$ flux is not detected. Despite the above issues, we test to see if there are systematic differences between the mass estimates of warm H_2 for the individual objects in our sample. We estimate the total H_2 mass as

$$M_{\text{tot}} = \frac{4}{3} M_o, \quad (9)$$

where M_o is the mass of the gas in the ortho state,

$$M_o = m_{\text{H}_2} N_T, \quad (10)$$

with m_{H_2} being the mass of an H_2 molecule and N_T the total number of molecules. The total number of molecules in the J^{th} state is $N_T = N_J/f_J$, where f_J is the partition function for the J^{th} state,

$$f_J = \frac{g_J \exp[-E_J/kT_{\text{exc}}]}{\sum_{J_i, \text{ortho}} g_{J_i} \exp[-E_{J_i}/kT_{\text{exc}}]} \quad (11)$$

where i indexes the H_2 transitions.

We fit H_2 excitation diagrams (E_J versus $\log(N_i/g_i)$) to find

the warm and warmer gas components, which uses a two component fit. Most of the pure-rotational H_2 transitions are weak detections. Using only two components can be highly degenerate and difficult to constrain without $\text{H}_2\text{S}(0)$ detections or stringent upper limits (Higdon et al. 2006; Roussel et al. 2007; Hill & Zakamska 2014; Petric et al. 2018). Due to low detection rates of $\text{H}_2\text{S}(0)$ in the majority of IRS low-resolution spectra, most two-temperature decomposition methods use upper limits of $\text{H}_2\text{S}(0)$, so their mass estimates are rough approximations. We perform a two-temperature decomposition on the H_2 excitation diagrams of our individual spectra. We only use spectra with at least two detected H_2 transitions and include upper limits for non-detections. For objects where only the $\text{H}_2\text{S}(1)$ and $\text{H}_2\text{S}(3)$ are detected, we assume a single temperature distribution. We also test if an ortho-to-para ratio (OPR) of 3 is valid, and if not we calculate the OPR via

$$\text{OPR} = \frac{\text{OPR}_{\text{high } T} \sum_o (2I_o + 1)(2J_o + 1) \exp[-E_o/kT_{\text{exc}}]}{3 \sum_p (2I_p + 1)(2J_p + 1) \exp[-E_p/kT_{\text{exc}}]} \quad (12)$$

where o, p denote ortho and para respectively and I_p, I_o are 0 and 1. $\text{OPR}_{\text{high } T}$ is equal to OPR in the high-temperature limit, i.e. $T > 200$ K, $\text{OPR} = 3$.

In the high-temperature OPR case we perform a Levenberg-Marquardt fitting algorithm (Markwardt 2009) to determine the parameters of the warm and warmer components (T_{warm} - lower temperature, T_{warmer} - upper temperature). We calculate the mass and column density (as described in Equation 9–Equation 11) of the warm and warmer component. In Table 7 we provide the derived mean temperatures and total mass fractions of two gas distributions for AGN and SF dominated galaxies via two-temperature decomposition. We find the distribution parameters of the AGN, SF dominated galaxies to be statistically indistinguishable from one another. As mentioned earlier, a small minority of our sample has

Table 7. (Method 1A) Derived Mean Temperatures and Masses Fractions of Two Gas Distributions for Individual Galaxies via Two-Temperature Decomposition: columns 1, 2, and 3 indicate the warm component temperature, warmer component temperature, and mass fraction of the warmer component to the total mass respectively. The rows indicate AGN, SF dominated as defined by $\text{EQW}[\text{PAH } 6.2 \mu\text{m}] < 0.27 \mu\text{m}$, $\text{EQW}[\text{PAH } 6.2 \mu\text{m}] > 0.54 \mu\text{m}$ respectively.

Class	T_{warm} (Median, K)	T_{warmer} (Median, K)	$\frac{M_{\text{warmer}}}{M_{\text{warm}} + M_{\text{warmer}}}$
AGN-Dominated	198.3 ± 31.2	522.1 ± 169.4	0.13 ± 0.06
SF-Dominated	192.9 ± 34.9	519.6 ± 276.0	0.11 ± 0.08

more than two 3σ H_2 detections. This severely affects the efficacy of the two-temperature decomposition method.

Two Temperature Decomposition Using a Marginalized Likelihood Analysis: The standard two-temperature decomposition uses a minimum chi-squared to determine the optimal fit to the excitation diagram. Minimizing chi-squared in this case is equivalent to maximizing the likelihood. As noted earlier, the decomposition of the excitation diagram into two populations can be degenerate due to the covariances between the slope of the warm and warmer H_2 distribution. This motivates method (1B) - two temperature decomposition using a marginalized likelihood analysis, where we construct an algorithm which uses the entirety of the likelihood function. The (1B) algorithm infers the ratio of warmer H_2 to warm H_2 by integrating over all possible values of the other parameters (e.g total mass). Unlike (1A), we treat the warm gas component and the total mass as a nuisance parameter. This allows us to fully examine the likelihood function of the parameter we care most about: the warmer component. The warmer component includes transitions that require more excitation energies than are typically found in PDRs. We hypothesize the greatest difference between AGN and SF dominated galaxies will be within these states. We first select targets where the signal-to-noise ratio of the PAH $6.2 \mu\text{m}$ line luminosity is at least 3, the $\text{H}_2\text{S}(0)$, $\text{H}_2\text{S}(1)$, $\text{H}_2\text{S}(2)$, $\text{H}_2\text{S}(3)$, and $\text{H}_2\text{S}(5)$ lines all fall within the observed wavelength range, and the signal-to-noise ratio of the H_2 line luminosities is at least 2. We convert the line luminosities and luminosity uncertainties to column densities and column density uncertainties. We do not replace marginal detections or non-detections with upper limits and instead keep the reported best-fit column densities and column density uncertainties.

We model each set of column densities as the superposition of a warm component and a warmer component. We parametrize the relative amplitudes of the two components in terms of a ratio of column densities, $r(h) \equiv N_{\text{warmer}, J=2} / N_{\text{warm}, J=2}$. We assign both components the same, possibly non-equilibrium, ‘local’ (i.e. per-level, the quantity which is equal to $3/4$ at ortho-to-para equilibrium regardless of the temperature) ortho-to-total fraction $f(o)$. We restrict the temperature T_{warm} of the warmer component to be non-zero. We parametrize the temperature of the warmer component as $T_{\text{warmer}} = T_{\text{warm}} + \Delta T$, where we restrict ΔT to be non-zero. The likelihood function (and posterior probability distribution) of this model can take on a variety of shapes depending on which transitions we can detect at high signal-to-noise ratios.

To assess the uncertainties on the parameters, we generate samples from the posterior probability distribution using

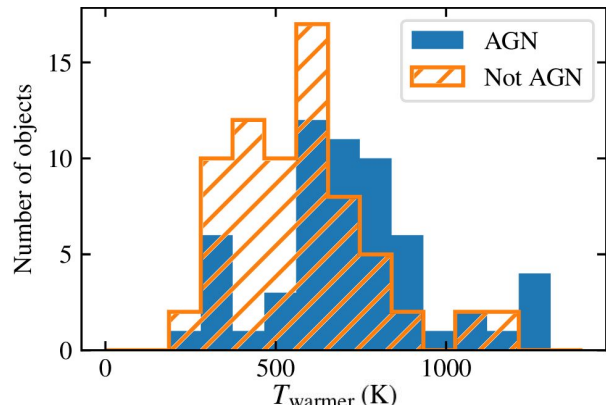


Figure 13. (Method 1B) - Two-Temperature Decomposition Likelihood Analysis: warmer component temperature distribution histogram. The blue bins and striped orange bins are the AGN-dominated and star-formation dominated sub-samples of galaxies respectively.

Markov chain Monte Carlo (MCMC). We have found that analytically marginalizing over the absolute amplitude dramatically improves convergence and mixing of MCMC, so we do not report any absolute column densities or masses. Instead, we utilize the ‘local’ ortho-to-total fraction $f(o)$; the ortho-to-para ratio $\text{OPR} \equiv \sum N_{J_{\text{odd}}} / \sum N_{J_{\text{even}}}$; the ratio of warm to warmer component column densities in the $J = 2$ level $r(h)$; the warmer column density fraction relative to the total amount of emitting H_2 $f(\text{warmer}) = N_{\text{warmer}} / (N_{\text{warm}} + N_{\text{warmer}})$; the warm and warmer component temperatures T_{warm} and T_{warmer} ; and the column density-weighted average temperature T_{avg} .

We find that AGN-dominated galaxies typically have higher T_{warmer} than SF-dominated galaxies (Figure 13). The difference between the two distributions is apparent by eye and is significant according to a two-sample KS test. The distributions of all other parameters reported from this analysis are consistent with being the same in the AGN-dominated and SF-dominated sub-samples, once again according to a two-sample KS test.

Galaxies are complex systems, and in spatially unresolved mid-infrared spectroscopy, a given warm H_2 transition represents the sum of different populations of H_2 gas at different locations within a galaxy. In methods (1A) and (1B), we separate a warm and warmer H_2 gas component. This helps provide a more physical H_2 gas parameter estimation, but this method suffers from a serious drawback; it requires well measured H_2 transitions to accurately sample a wide range of excitation temperatures. The flux limited nature of H_2 detections makes secure temperature component estimates difficult, thus it is unsurprising we do not find a difference between AGN, not-AGN dominated sub-samples in (1B). (1B) attempts to overcome some of the technical problems of (1A), i.e. line-fitting noisy or under-sampled data by using the entirety of the likelihood function and marginalizing over parameters that we are less interested in. In this case, we do find a statistical temperature difference in the warmer gas component: AGN have higher temperatures in their warmer component versus not-AGN dominated host galaxies. In the next section, we test if properties within a given line transition is statistically separable between the AGN and not-AGN dominated sub-samples.

3.5 Warm Molecular Hydrogen Excitation Temperatures

Excitation temperatures per line pair: For the unstacked spectra, we first utilize method (2a) which is the simplest approach of calculating the excitation temperatures via the following pairs of lines: (H₂S(0), H₂S(2)), (H₂S(3), H₂S(1)), (H₂S(5), H₂S(3)), and (H₂S(7), H₂S(5)). Using only transitions with $> 2\sigma$ significance, we calculate the excitation temperatures (T_{exc}) of the gas in a given transition via pairs of lines. We compare the distributions of the temperatures between a sample of AGN-dominated and SF-dominated galaxies. As before, we define an AGN-dominated (SF-dominated) galaxy as one with EQW[PAH 6.2 μm] $< 0.27 \mu\text{m}$ (EQW[PAH 6.2 μm] $> 0.54 \mu\text{m}$). We do not include the 90 objects that have comparable AGN and SF contribution. Because the majority of the spectra do not have enough detections to confidently measure the ortho-to-para ratio, we choose to only measure excitation temperatures between states of the same parity. The column density, N_{J+2} , in the upper level of each transition assuming the gas is in local thermal equilibrium defined as

$$N_{J+2} = \frac{4\pi D_L^2 F_J}{A_{J+2 \rightarrow J}(E_{J+2} - E_J)} \quad (13)$$

where D_L is the luminosity distance, F_J is the line flux, $(E_{J+2} - E_J)$ is the energy of the transition, and A_J and A_{J+2} are the Einstein coefficients (Turner et al. 1977). The energy levels are

$$E_J = 85.35 \text{ K} \cdot k_B J(J+1) - 0.068 \text{ K} \cdot k_B J^2(J+1)^2, \quad (14)$$

where k_B is the Boltzmann constant. T_{exc} is then estimated via the relationship between N_J , g_J , E_J , and T_{exc} ,

$$\frac{N_J}{g_J} = \exp\left(-\frac{E_J}{k_B T_{\text{exc}}}\right), \quad (15)$$

where $g_J = 2J+1$ for even J and $g_J = 3(2J+1)$ for odd J assuming an equilibrium ortho-to-para ratio. The excitation temperature from transition pairs of the same parity is $T_{u,l} = (E_u - E_l)/\ln(N_l/N_u \times g_u/g_l)$ where u and l correspond to the upper and lower transition respectively. For example, the excitation temperature via the pair of transitions H₂S(3), H₂S(1) is represented as $T_{3,1}$.

As shown in Table 8, we find the mean T_{exc} of the AGN dominated sub-sample is consistently higher than the SF-dominated sub-sample. For this specific analysis method, we are hesitant to derive deeper physical meaning from these values due to the exclusive selection criteria of the detections for each pair of transitions. For example, $T_{2,0}$ requires 2σ detections of both $f_{\nu}[\text{H}_2\text{S}(0)]$ and $f_{\nu}[\text{H}_2\text{S}(2)]$, and $T_{3,1}$ requires 2σ detections of both $f_{\nu}[\text{H}_2\text{S}(1)]$ and $f_{\nu}[\text{H}_2\text{S}(3)]$, but there are only 20 objects that satisfy both the $T_{3,1}$ and $T_{2,0}$ selection criteria. For the few objects that do satisfy all of the criteria, the errors on the mean temperatures are large (see Table 8).

We then employ method (2a) on the stacked spectra. We calculate excitation temperatures for the 50 stacked spectra in which the H₂S(0), H₂S(1), H₂S(2), H₂S(3), H₂S(5) are at least 2σ detections. We exclude the H₂S(7) transition from the stacked spectral excitation temperature analysis due to the high noise in this region in the stacks. We calculate the following temperatures using the following pairs of transitions that have the same parity: $T_{2,0}$, $T_{3,1}$, and $T_{5,3}$. We perform a locally weighted regression, a type of non-parametric regression that joins a series of local polynomial regressions (Cleveland 1979). We choose this method because the raw data do not display linear behaviour, and we have no reason to assume the temperature evolution as a function of AGN MIR dominance would be linear.

Table 8. (Method 2A) - Excitation Temperature Analysis to Find Mean Temperatures of Individual 2σ transition temperature detections of the AGN, not-AGN sub-samples: column 1 indicates the excitation temperature $T_{u,l}$, column 2 and column 3 are the AGN sub-sample (EQW[PAH 6.2 μm] $< 0.27 \mu\text{m}$) temperatures and the not-AGN dominated sub-sample (EQW[PAH 6.2 μm] $> 0.27 \mu\text{m}$) temperatures respectively, and column 4 is the number of objects with 2σ detections in each sub-sample.

$T_{u,l}$	not-AGN (Mean, K)	AGN (Mean, K)	Number (not-AGN, AGN)
$T_{2,0}$	168.6 \pm 11.2	171.9 \pm 12.0	10, 12
$T_{3,1}$	304.9 \pm 17.2	306.9 \pm 19.9	244, 116
$T_{5,3}$	771.5 \pm 114.3	946.1 \pm 102.8	28, 47
$T_{7,5}$	1214.7 \pm 185.4	1490.7 \pm 212.5	13, 21

We calculate the central tendency of our three sets of excitation temperatures for discrete bins of EQW[PAH 6.2 μm] in Figure 14. The values to the left of the empirical threshold of AGN activity (i.e. EQW[PAH 6.2 μm] $< 0.27 \mu\text{m}$) are quite scattered, yielding a flat relationship. Despite the scatter, we find a ~ 200 K difference in $T_{5,3}$ between the most AGN dominated galaxies versus most star-formation dominated systems. Due to the normalization of the stacks, we cannot calculate the H₂ mass. The stacks also rely wholly on the fundamental assumption that the EQW[PAH 6.2 μm] is the sole separator between galaxy types. This assumption is useful for comparing AGN selection criteria, but the potential nuances between galaxy types and H₂ emission within galaxies of similar EQW[PAH 6.2 μm] would be lost.

Hierarchical modelling of the excitation temperature distribution: Methods (1A), (1B), and (2A) rely on measuring accurate excitation temperatures for galaxies individually. However, method (2b), hierarchical modelling of the excitation temperature distribution within a given sub-sample, can infer the distribution of excitation temperatures within the SF-dominated and AGN-dominated sub-samples without needing to measure excitation temperatures for any individual galaxy. A hierarchical model is one in which inference is done simultaneously over the parameters describing the population and the parameters describing the members of the population (see Gelman et al. 2013 for an in depth introduction to hierarchical modelling and Hogg et al. 2010 for a short but carefully explained astronomical example).

Hierarchical modelling is more appropriate than doing an excitation analysis on a stacked spectrum for determining the mean excitation temperature of a population. This is the case because excitation temperature is non-linearly related to the observable, flux. As a result of this non-linearity, the excitation temperature of the mean (or median) of a collection of spectra will not, in general, be equal to the mean of the excitation temperatures of the individual spectra even when no noise is present. Our hierarchical model computes the mean of a collection of excitation temperatures derived from noisy flux measurements in a way that correctly accounts for the non-Gaussianity of their uncertainties.

A non-hierarchical modelling approach to characterizing the distribution of excitation temperatures in a population could be first calculating temperatures for each individual galaxy, then averaging those individual temperatures together. Then, the parameters describing the individual galaxies are fixed to some value which is then used to compute a population-level quantity. In hierarchical modelling, the parameters of individual galaxies are not held fixed.

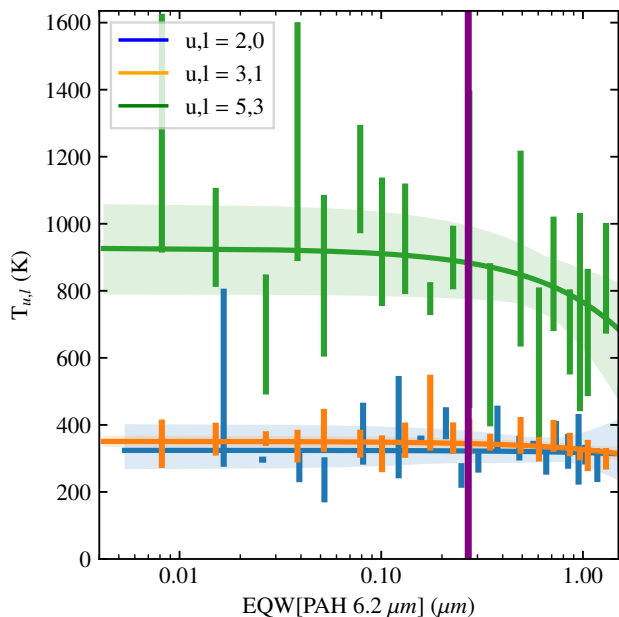


Figure 14. (Method 2A - Stacked Spectra) Excitation temperature evolution as a function of EQW[PAH 6.2 μm]. We calculate the $T_{u,l}$ using the Boltzmann relation. The vertical purple line is the empirical PAH 6.2 μm equivalent width upper boundary of AGN dominance. The solid lines are the smoothed regression of all the data points for the three different $T_{u,l}$ measurements. We plot the central tendency and full range of $T_{u,l}$ measurements for discrete bins of EQW[PAH 6.2 μm]. The largest temperature difference occurs in the highest transition pair $T_{u,l}$.

Parameters that vary in our hierarchical model include both the excitation temperature of each galaxy and the parameters of the distribution of excitation temperatures in the population. By integrating over all possible values of the individual galaxy parameters, we get a more robust estimate of the population-level parameters.

If we do not know the parameters of the prior distribution ahead of time, we can attempt to infer the prior parameters and the individual galaxy parameters at the same time. This approach is particularly useful when one has a large sample of galaxies, most of which have poorly constrained parameters. The black curve in the middle panel of Figure 15 is an example of a poorly constrained excitation temperature likelihood function. By combining information from the black curve with information from the better-constrained red curve and many others, we can infer a prior over excitation temperatures. This prior is shown as a dashed grey curve in the third panel of the same figure.

The hierarchical Bayesian modelling method requires that we assume a functional form for the sample-level distribution. We assume the distribution of T_{exc} within each sample is a Gaussian with mean and standard deviation $T_{\text{exc,mean}}$ and $T_{\text{exc},\sigma}$. If the T_{exc} of each galaxy in a sample were known to infinite precision, the probability of a $(T_{\text{exc,mean}}, T_{\text{exc},\sigma})$ pair would be the product of a normal distribution with mean $T_{\text{exc,mean}}$ and standard deviation $T_{\text{exc},\sigma}$. Instead, for each galaxy in our sample we have a likelihood function $\mathcal{L}(T_{\text{exc}})$ over all possible values of T_{exc} . The probability of a $(T_{\text{exc,mean}}, T_{\text{exc},\sigma})$ pair as determined from the spectrum of a single galaxy is now given by an integral over the product of that galaxy's T_{exc} likelihood function and the (normal) distribution of T_{exc} values

in our sample:

$$\int_0^{\infty} \frac{1}{\sqrt{2\pi}T_{\text{exc},\sigma}} \exp\left[-\frac{(T_{\text{exc,mean}} - T_{\text{exc}})^2}{2T_{\text{exc},\sigma}^2}\right] \mathcal{L}(T_{\text{exc}}) dT_{\text{exc}}. \quad (16)$$

The probability of a specific $(T_{\text{exc,mean}}, T_{\text{exc},\sigma})$ determined from all the galaxies in our sample is the product of that integral evaluated for each galaxy. Our inference consists of mapping out the probability of $T_{\text{exc,mean}}$ and $T_{\text{exc},\sigma}$ given the spectra in each sample.

We use MCMC with the EMCEE implementation of the affine invariant ensemble sampler (Foreman-Mackey et al. 2013) to estimate the expectation value and standard deviation of $T_{\text{exc,mean}}$ for each pair of transitions (Figure 16). The excitation temperatures between the $\text{H}_2\text{S}(2)$, $\text{H}_2\text{S}(0)$ and $\text{H}_2\text{S}(3)$, $\text{H}_2\text{S}(1)$ energy levels are the same in both samples while the excitation temperatures between the higher-energy $\text{H}_2\text{S}(5)$, $\text{H}_2\text{S}(3)$ and $\text{H}_2\text{S}(7)$, $\text{H}_2\text{S}(5)$ energy levels are significantly higher in AGN dominated galaxies than in star-formation dominated galaxies.

4 DISCUSSION

We find an excess of H_2 emission and a statistically significant temperature difference in the warmer gas component in AGN dominated galaxies. We find AGN dominated host galaxies on average have at least 5 times greater H_2 to PAH ratios than SF-dominated host galaxies. In order to understand the nature of this excess H_2 emission, we calculate the temperature of the warm H_2 gas using two different approaches: (1) using all of the H_2 lines simultaneously to determine a warm and warmer temperature component and (2) calculating excitation temperatures of H_2 line pairs of equal parity. The two-temperature decomposition via likelihood analysis method shows no statistical difference between the AGN and not-AGN dominated sub-samples for the warm component, but the warmer component shows a 1σ 200 K median temperature difference in the AGN dominated and not-AGN dominated sub-samples. For (2A), the unstacked, stacked spectra show a roughly 2σ $T_{\text{exc,mean}}$ difference for $(u, l) = (5, 3)$ of 175.0 K, 210.0 K respectively. The unstacked spectra also show a roughly 2σ 276.0 K difference of $T_{\text{exc,mean}}$ for $(u, l) = (7, 5)$ between the AGN, not-AGN dominated sub-samples. (2B), the hierarchical Bayesian model, shows a roughly 2σ $T_{\text{exc,mean}}$ difference for $(u, l) = 5, 3$, $(u, l) = 7, 5$ of 120.0 K, 200.0 K between the AGN dominated and not-AGN dominated sub-samples, respectively.

The warm gas component (100 K – 300 K), is dominated by SF processes in both local IR AGN and not-AGN dominated host galaxies (Rigopoulou et al. 2002; Higdon et al. 2006; Roussel et al. 2007). This leads to a strong correlation between the amount of H_2 and PAH emission and a nearly constant ratio between the two, as both are by-products of star-formation. Petric et al. (2018) use high-resolution IRS spectra to find a population of LIRGs with enhanced H_2 and broader, spectrally resolved H_2 lines. They speculate that the broader profiles are due to bulk flows associated with AGN or high-mass star-formation. They find that AGN appear to have warmer gas and dust than non-AGN. However, few of their spectra have detections higher than $\text{H}_2\text{S}(3)$, so they are unable to conduct the same thorough analysis we perform here. In our sample of objects that have 2σ or greater detections of $\text{H}_2\text{S}(3)$, PAH[11.3 μm], and PAH[6.2 μm], we find the most star-formation dominated objects (EQW[PAH 6.2 μm] > 1.0 μm , 134 objects) have H_2 to PAH ratios of 0.016 ± 0.001 . For objects that are still considered star-formation dominated (EQW[PAH 6.2 μm]

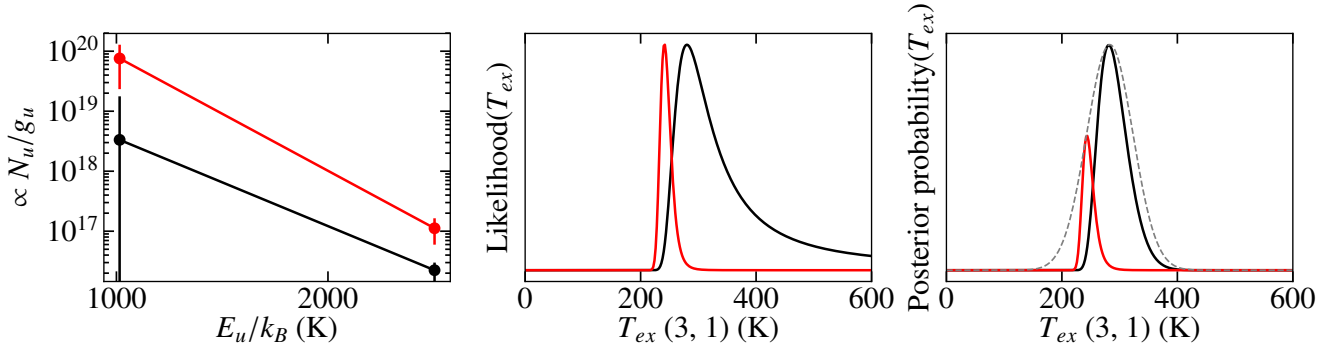


Figure 15. (Method 2B) – Example distribution mapping: The first panel shows the excitation diagram using H₂S(1) and H₂S(3) for two different random objects in our sample. The red line corresponds to a 3 σ detection in both the S(1) and S(3) transitions. The black line corresponds to an object with a well constrained S(3) value, but a 1 σ H₂S(1) detection. In the second panel, we show the likelihoods of the two objects. After finding the likelihoods for every detection for a given same parity pair, we then use the averages of the likelihoods to re-run the model, providing a more robust estimate of the mean temperature of the transition. In this example both objects are in our sample, and the grey-dashed line represents the estimated temperature distribution for a given transition for this sample.

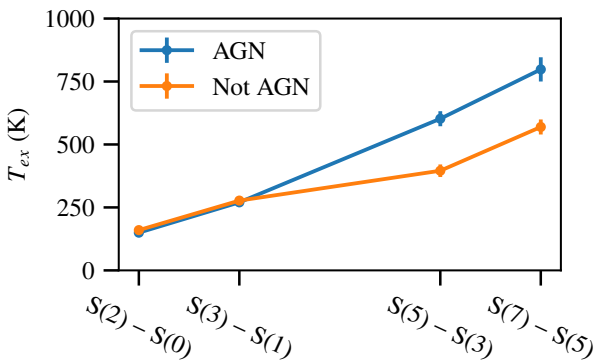


Figure 16. (Method 2B) - Excitation temperature differences between AGN and non-AGN: We use a hierarchical Bayesian model to compute the excitation temperature distribution for the pairs of transitions listed in the figure within the AGN, non-AGN dominated subsamples. We find that the mean excitation temperatures of the higher H₂ transitions distributions are higher in sources with an AGN than in sources without an AGN. The blue line represents the subsample with EQW[PAH 6.2 μ m] < 0.27 μ m and the orange line shows all other sources. The points represent the expectation values for each distribution with one standard-deviation error-bars.

> 0.54 μ m & EQW[PAH 6.2 μ m] < 1.0 μ m, 104 objects), we find H₂ to PAH ratios of 0.050 ± 0.002 . These values are consistent with Roussel et al. (2007) and Stierwalt et al. (2014) results for star-forming dominated galaxies.

In ULIRGs, different authors draw different conclusions about the origins of the excess H₂ emission. Although we are not splitting our sample in bins of IR, up to 58 per cent of ULIRGs contain an AGN (Yuan et al. 2010). Higdon et al. (2006) find that the masses of warm H₂ in ULIRGs are not correlated with the AGN contribution to the MIR emission, so they suggest that in ULIRGs the warm H₂ emission comes from PDRs. However, using the H₂ to PAH ratio as an indicator for warm H₂ excess, Zakamska (2010) and Hill & Zakamska (2014) do find more H₂ than is expected from star-formation alone. Observations of H₂ in AGN host galaxies with radio jets suggest that kinetic energy dissipation by shocks or cosmic rays can produce a factor of 300 or larger H₂ to PAH values than

normal star-forming galaxies (Ogle et al. 2010). Of the most AGN dominated objects (EQW[PAH 6.2 μ m] < 0.1 μ m, 51 objects) we find H₂ to PAH ratios of 0.130 ± 0.007 . For objects that are still considered AGN dominated with EQW[PAH 6.2 μ m] > 0.1 μ m & EQW[PAH 6.2 μ m] < 0.27 μ m (85 objects), we find H₂ to PAH ratios of 0.090 ± 0.008 . These values are consistent with Hill & Zakamska (2014) results for AGN dominated galaxies.

In the literature, there is a lack of association between the temperature of the warm H₂ and AGN activity. The greatest potential observable effect on the H₂ gas would be seen in the higher temperature transitions, since these transitions are more difficult to excite from SF processes. These transitions are also difficult to observe, and thus, methods that rely on high signal to noise fluxes will be less effective. Methods that find excitation temperatures without separating the different temperatures have the problem of different components contributing to the flux of a given transition. For transitions that are easily excited by multiple physical processes, a single temperature would be inaccurate, but it has been found that the warmer gas component contributes on average only a few percent compared to the warm component in galaxies where SF dominates (Higdon et al. 2006; Roussel et al. 2007). The H₂S(3), H₂S(5), and H₂S(7) transitions all constrain the warmer temperature component of the gas, and in particular H₂S(5), H₂S(7) transitions have relatively little contribution from the warm gas component. This motivates methods (2a) and (2b), where a single temperature is assumed, and we focus only on the difference between the higher temperature transitions. The results of (2a) and (2b) show significant differences in $T_{\text{exc,mean}}$ for $(u,l) = 5,3$, $(u,l) = 7,5$ between the AGN, not-AGN sub-samples. These higher transitions require higher excitation temperatures, and have higher critical densities (Neufeld et al. 2006). Although we cannot completely rule out density effects, our results show an average 200 K temperature difference in the transitions the AGN are likely to affect most. In the remaining text, we postulate the origin of the excess emission.

Observations of AGN-dominated ULIRGs show evidence of fast outflows of molecular gas that are spatially extended on kilo-parsec scales (Feruglio et al. 2010; Spoon et al. 2013; Rupke & Veilleux 2013; Ciccone et al. 2014; Aalto et al. 2015). Outflows can deplete galaxies of their gas and quench star-formation on timescales of 10^6 – 10^8 years (Sturm et al. 2011; Liu et al. 2013; Brusa et al. 2015; Rupke et al. 2017). The origin of these molec-

ular outflows is unclear, but one possibility is that radiative winds launched from regions close to the AGN create the outflow. The winds can provide an efficient way to couple the AGN's energy to the ISM (Tombesi et al. 2015). Large fractions of kinetic energy are deposited in the ISM and can accelerate existing molecular gas. The propagating outflow interacts with the ISM via heating, entraining, and/or shocking gas clouds in its path (Cecil et al. 2002; Rupke et al. 2017). A wide range of physical conditions exists in the outflow. One of the phases of the outflow is partially ionized regions where [O I] λ 6300 Å and [Fe II] emission lines are produced.

In ULIRGs, Hill & Zakamska (2014) find a strong correlation between warm H₂ and the ionized gas, suggesting that the excess warm H₂ is excited in the same regions of outflow driven shocks. An alternative possibility is that the molecules form in the material swept up by the wind. Richings & Faucher-Giguère (2018a) simulated an AGN wind interacting with a uniform medium and explored the possibility of in-situ molecule formation. Using a radiative transfer model, they computed the amount of warm H₂ emission. The H₂S(0), H₂S(1), H₂S(2), and H₂S(3) level populations derived from the in-situ molecule formation AGN wind model described in Richings & Faucher-Giguère (2018a,b) indicate excitation temperatures of 400–547 K. This agrees with our result that AGN dominated galaxies have a distinct population of H₂. AGN driven jets, shocks, and winds are not the only processes than can lead to the excitation of H₂ in the warm phase. Shocks produced by young stars, supernovae, and galaxy collisions can also excite these transitions. Any shock-producing mechanism related to solely SF processes will also occur in our SF dominated sub-sample. Thus, we postulate that the warm excess H₂ emission and temperature difference is a direct consequence of AGN activity.

5 SUMMARY AND CONCLUSION

We use MIR spectroscopy to evaluate the relationship between AGN and the ISM of their host galaxies. We analyse 2,015 objects low-resolution spectra (Lebouteiller et al. 2011) with published spectroscopic redshifts (Hernán-Caballero et al. 2016). We correct mismatches between the different spectral orders and check the flux calibration of the spectra using *WISE* photometry. We measure rotational H₂ transitions, PAH emission in the 6.2, 7.7, and 11.3 μ m bands, and summarize our results as follows:

(i) We use the EQW[PAH 6.2 μ m] to separate our sample galaxies where the AGN contributes more than 50 per cent of the MIR luminosity and galaxies where star-formation contributes more than 50 per cent of the MIR luminosity.

(ii) We find that the PAHs in AGN-dominated galaxies have a wider range of ionizations and sizes, and the effect of silicate absorption on grain size tracers is different for AGN dominated galaxies vs SF dominated galaxies. This may imply that the ISM in AGN hosts is more complex than the ISM of SF-dominated galaxies; without analysing the host morphologies we cannot separate the impact of the AGN on the ISM from that of any gravitational interactions.

(iii) In AGN-dominated systems, we find an excess of molecular H₂ emission relative to what we would measure if the molecular H₂ originated solely from PDRs.

(iv) We find a 120 K temperature difference in $T_{5,3}$ between AGN-dominated galaxies and SF-dominated targets. The difference in $T_{7,5}$ between these targets increases to 200 K. This may suggest that the AGN heats the molecular gas in the inner \sim 5 kpc probed by the IRS observations.

ACKNOWLEDGEMENTS

We thank D.A. Neufeld, T. Heckman, and N. Flagey for useful discussions. ELL is supported by the Maryland Space Grant Consortium. NLZ acknowledges support by Johns Hopkins University through the Catalyst Award and by the Institute for Advanced Study through the Deborah Lunder and Alan Ezekowitz Founders' Circle Membership. This research has made use of the NASA/IPAC Infrared Science Archive, which is operated by the Jet Propulsion Laboratory, California Institute of Technology, under contract with the National Aeronautics and Space Administration. This publication makes use of data products from the *Wide-field Infrared Survey Explorer*, which is a joint project of the University of California, Los Angeles, and the Jet Propulsion Laboratory/California Institute of Technology, funded by the National Aeronautics and Space Administration. This publication makes use of data products from the Two Micron All Sky Survey, which is a joint project of the University of Massachusetts and the Infrared Processing and Analysis Center/California Institute of Technology, funded by the National Aeronautics and Space Administration and the National Science Foundation. We acknowledge the extensive use of the following Python packages: PANDAS, SCIPY, IPYTHON, MATPLOTLIB, SCI-KIT LEARN, EMCEE (McKinney 2010; Jones et al. 01 ; Pérez & Granger 2007; Hunter 2007; Pedregosa et al. 2012; Foreman-Mackey et al. 2013, respectively). This research made use of ASTROPY, a community-developed core Python package for Astronomy (Astropy Collaboration et al. 2013).

REFERENCES

- Aalto S., et al., 2015, *A&A*, **584**, A42
 Allamandola L. J., Tielens A. G. G. M., Barker J. R., 1989, *ApJS*, **71**, 733
 Appleton P. N., et al., 2006, *ApJ*, **639**, L51
 Armus L., et al., 2006, *ApJ*, **640**, 204
 Armus L., et al., 2007a, *ApJ*, **656**, 148
 Armus L., et al., 2007b, *ApJ*, **656**, 148
 Assef R. J., et al., 2013, *ApJ*, **772**, 26
 Assef R. J., Stern D., Noirotd G., Jun H. D., Cutri R. M., Eisenhardt P. R. M., 2018, *ApJS*, **234**, 23
 Astropy Collaboration et al., 2013, *A&A*, **558**, A33
 Baldwin J. A., Phillips M. M., Terlevich R., 1981, *PASP*, **93**, 5
 Blecha L., Snyder G. F., Satyapal S., Ellison S. L., 2018, *MNRAS*, **478**, 3056
 Brandl B. R., et al., 2006, *ApJ*, **653**, 1129
 Brusa M., et al., 2015, *MNRAS*, **446**, 2394
 Buat V., Deharveng J. M., 1988, *A&A*, **195**, 60
 Burton M. G., Hollenbach D. J., Tielens A. G. G., 1992, *ApJ*, **399**, 563
 Calzetti D., et al., 2007, *ApJ*, **666**, 870
 Cecil G., Bland-Hawthorn J., Veilleux S., 2002, *ApJ*, **576**, 745
 Cicone C., Feruglio C., Maiolino R., Fiore F., Piconcelli E., Menci N., Ausel H., Sturm E., 2012, *A&A*, **543**, A99
 Cicone C., et al., 2014, *A&A*, **562**, A21
 Cleveland W. S., 1979, *Journal of the American Statistical Association*, **74**, 829
 Cluver M. E., et al., 2010, *ApJ*, **710**, 248
 Cresci G., et al., 2015, *A&A*, **582**, A63
 Desai V., et al., 2007, *ApJ*, **669**, 810
 Diamond-Stanic A. M., Rieke G. H., 2010, *ApJ*, **724**, 140
 Donley J. L., et al., 2012, *ApJ*, **748**, 142
 Draine B. T., 2003, *ApJ*, **598**, 1017
 Draine B. T., Li A., 2007, *ApJ*, **657**, 810
 Eisenhardt P. R. M., et al., 2012, *ApJ*, **755**, 173
 Elitzur M., 2012, *ApJ*, **747**, L33
 Elvis M., et al., 1994, *ApJS*, **95**, 1
 Fabian A. C., 1999, *MNRAS*, **308**, L39

- Fabian A. C., 2012, *ARA&A*, 50, 455
- Feruglio C., Maiolino R., Piconcelli E., Menci N., Aussel H., Lamastra A., Fiore F., 2010, *A&A*, 518, L155
- Foreman-Mackey D., Hogg D. W., Lang D., Goodman J., 2013, *PASP*, 125, 306
- Gelman A., Carlin J. B., Stern H. S., Dunson D. B., Vehtari A., Rubin D. B., 2013, *Bayesian Data Analysis*, Third Edition (Chapman & Hall/CRC Texts in Statistical Science). Chapman and Hall/CRC, <http://www.stat.columbia.edu/~gelman/book/>
- Genzel R., et al., 1998, *ApJ*, 498, 579
- Greene J. E., Zakamska N. L., Ho L. C., Barth A. J., 2011, *ApJ*, 732, 9
- Greene J. E., Zakamska N. L., Smith P. S., 2012, *ApJ*, 746, 86
- Guillard P., et al., 2012, *ApJ*, 749, 158
- Gürkan G., Hardcastle M. J., Jarvis M. J., 2014, *MNRAS*, 438, 1149
- Haan S., et al., 2011, *ApJS*, 197, 27
- Heckman T. M., Best P. N., 2014, *ARA&A*, 52, 589
- Hernán-Caballero A., Spoon H. W. W., Lebouteiller V., Rupke D. S. N., Barry D. P., 2016, *MNRAS*, 455, 1796
- Higdon S. J. U., Armus L., Higdon J. L., Soifer B. T., Spoon H. W. W., 2006, *ApJ*, 648, 323
- Hill M. J., Zakamska N. L., 2014, *MNRAS*, 439, 2701
- Hogg D. W., Myers A. D., Bovy J., 2010, *ApJ*, 725, 2166
- Hollenbach D. J., Tielens A. G. G. M., 1999, *Reviews of Modern Physics*, 71, 173
- Hopkins P. F., Hernquist L., Cox T. J., Di Matteo T., Robertson B., Springel V., 2006, *ApJS*, 163, 1
- Houck J. R., et al., 2004, *ApJS*, 154, 18
- Hunter J. D., 2007, *Computing In Science & Engineering*, 9, 90
- Jarrett T. H., et al., 2011, *ApJ*, 735, 112
- Jensen J. J., et al., 2017, *MNRAS*, 470, 3071
- Jones E., Oliphant T., Peterson P., et al., 2001–, SciPy: Open source scientific tools for Python, <http://www.scipy.org/>
- Karouzos M., Woo J.-H., Bae H.-J., 2016, *ApJ*, 833, 171
- Kauffmann G., et al., 2003, *MNRAS*, 346, 1055
- King A., 2003, *ApJ*, 596, L27
- Kormendy J., Ho L. C., 2013, *ARA&A*, 51, 511
- Lacy M., et al., 2004, *ApJS*, 154, 166
- Lacy M., Petric A. O., Sajina A., Canalizo G., Storrie-Lombardi L. J., Armus L., Fadda D., Marleau F. R., 2007, *AJ*, 133, 186
- Lacy M., Ridgway S. E., Sajina A., Petric A. O., Gates E. L., Urrutia T., Storrie-Lombardi L. J., 2015, *ApJ*, 802, 102
- Laurent O., Mirabel I. F., Charmandaris V., Gallais P., Madden S. C., Sauvage M., Vigroux L., Cesarsky C., 2000, *A&A*, 359, 887
- Le Petit F., Nehmé C., Le Bourlot J., Roueff E., 2006, *ApJS*, 164, 506
- Lebouteiller V., Barry D. J., Spoon H. W. W., Bernard-Salas J., Sloan G. C., Houck J. R., Weedman D. W., 2011, *ApJS*, 196, 8
- Leger A., D'Hendecourt L., Defourneau D., 1989, *A&A*, 216, 148
- Li A., Draine B. T., 2001, *ApJ*, 554, 778
- Liu G., Zakamska N. L., Greene J. E., Nesvadba N. P. H., Liu X., 2013, *MNRAS*, 436, 2576
- Madau P., Dickinson M., 2014, *ARA&A*, 52, 415
- Markwardt C. B., 2009, in Bohlender D. A., Durand D., Dowler P., eds, *Astronomical Society of the Pacific Conference Series Vol. 411, Astronomical Data Analysis Software and Systems XVIII*. p. 251 ([arXiv:0902.2850](https://arxiv.org/abs/0902.2850))
- Marshall J. A., Herter T. L., Armus L., Charmandaris V., Spoon H. W. W., Bernard-Salas J., Houck J. R., 2007, *ApJ*, 670, 129
- Martínez-Sansigre A., Rawlings S., Lacy M., Fadda D., Marleau F. R., Simpson C., Willott C. J., Jarvis M. J., 2005, *Nature*, 436, 666
- Mateos S., et al., 2012, *MNRAS*, 426, 3271
- McKinney W., 2010, in van der Walt S., Millman J., eds, *Proceedings of the 9th Python in Science Conference*. pp 51 – 56
- Neškova M., Sirocky M. M., Nikutta R., Ivezić Ž., Elitzur M., 2008, *ApJ*, 685, 160
- Nesvadba N. P. H., Polletta M., Lehnert M. D., Bergeron J., De Breuck C., Lagache G., Omont A., 2011, *MNRAS*, 415, 2359
- Neufeld D. A., et al., 2006, *ApJ*, 649, 816
- O'Dowd M. J., et al., 2009, *ApJ*, 705, 885
- Ogle P., Boulanger F., Guillard P., Evans D. A., Antonucci R., Appleton P. N., Nesvadba N., Leipski C., 2010, *ApJ*, 724, 1193
- Ogle P., Davies J. E., Appleton P. N., Bertin-court B., Seymour N., Helou G., 2012, *ApJ*, 751, 13
- Pedregosa F., et al., 2012, *J. Mach. Learn. Res.*, 12, 2825
- Peeters E., Spoon H. W. W., Tielens A. G. G. M., 2004, *ApJ*, 613, 986
- Peeters E., Bauschlicher Jr. C. W., Allamandola L. J., Tielens A. G. G. M., Ricca A., Wolfire M. G., 2017a, *ApJ*, 836, 198
- Peeters E., Bauschlicher Jr. C. W., Allamandola L. J., Tielens A. G. G. M., Ricca A., Wolfire M. G., 2017b, *ApJ*, 836, 198
- Pérez F., Granger B. E., 2007, *Computing in Science and Engineering*, 9, 21
- Petric A. O., et al., 2011, *ApJ*, 730, 28
- Petric A. O., et al., 2018, preprint, p. [arXiv:1805.09926](https://arxiv.org/abs/1805.09926) ([arXiv:1805.09926](https://arxiv.org/abs/1805.09926))
- Reyes R., et al., 2008, *AJ*, 136, 2373
- Richings A. J., Faucher-Giguère C.-A., 2018a, *MNRAS*, 474, 3673
- Richings A. J., Faucher-Giguère C.-A., 2018b, *MNRAS*, 478, 3100
- Rigopoulou D., Kunze D., Lutz D., Genzel R., Moorwood A. F. M., 2002, *A&A*, 389, 374
- Roussel H., et al., 2007, *ApJ*, 669, 959
- Rowan-Robinson M., Crawford J., 1989, *MNRAS*, 238, 523
- Rupke D. S. N., Veilleux S., 2013, *ApJ*, 768, 75
- Rupke D. S. N., Gültekin K., Veilleux S., 2017, *ApJ*, 850, 40
- Sadjadi S., Zhang Y., Kwok S., 2015, *ApJ*, 807, 95
- Sales D. A., Pastoriza M. G., Riffel R., 2010, *ApJ*, 725, 605
- Sanders D. B., Phinney E. S., Neugebauer G., Soifer B. T., Matthews K., 1989, *ApJ*, 347, 29
- Sauvage M., Thuan T. X., 1992, *ApJ*, 396, L69
- Sauvage M., Thuan T. X., 1994, *ApJ*, 429, 153
- Shipley H. V., Papovich C., Rieke G. H., Dey A., Jannuzi B. T., Moustakas J., Weiner B., 2013, *ApJ*, 769, 75
- Silk J., Mamon G. A., 2012, *Research in Astronomy and Astrophysics*, 12, 917
- Silk J., Rees M. J., 1998, *A&A*, 331, L1
- Skrutskie M. F., et al., 2006, *AJ*, 131, 1163
- Smith J. D., Draine B., 2012, PAHFIT: Properties of PAH Emission, Astrophysics Source Code Library (ascl:1210.009)
- Smith J. D. T., et al., 2007, *ApJ*, 656, 770
- Spoon H. W. W., Marshall J. A., Houck J. R., Elitzur M., Hao L., Armus L., Brandl B. R., Charmandaris V., 2007, *ApJ*, 654, L49
- Spoon H. W. W., et al., 2013, *ApJ*, 775, 127
- Stern D., et al., 2005, *ApJ*, 631, 163
- Stern D., et al., 2012, *ApJ*, 753, 30
- Stierwalt S., et al., 2014, *ApJ*, 790, 124
- Stock D. J., Peeters E., 2017, *ApJ*, 837, 129
- Stone M., Veilleux S., Meléndez M., Sturm E., Graciá-Carpio J., González-Alfonso E., 2016, *ApJ*, 826, 111
- Sturm E., et al., 2011, *ApJ*, 733, L16
- Tielens A. G. G. M., 2005, *The Physics and Chemistry of the Interstellar Medium*. Cambridge University Press
- Tombesi F., Meléndez M., Veilleux S., Reeves J. N., González-Alfonso E., Reynolds C. S., 2015, *Nature*, 519, 436
- Trump J. R., et al., 2015, *ApJ*, 811, 26
- Turner J., Kirby-Docken K., Dalgarno A., 1977, *ApJS*, 35, 281
- Villar-Martín M., Arribas S., Emonts B., Humphrey A., Tadhunter C., Bessiere P., Cabrera Lavers A., Ramos Almeida C., 2016, *MNRAS*, 460, 130
- Weedman D. W., Feldman F. R., Balzano V. A., Ramsey L. W., Sramek R. A., Wu C.-C., 1981, *ApJ*, 248, 105
- Weedman D. W., et al., 2005, *ApJ*, 633, 706
- Weinberger R., et al., 2018, *MNRAS*, 479, 4056
- Wright E. L., et al., 2010, *AJ*, 140, 1868
- Wylezalek D., et al., 2017, *MNRAS*, 467, 2612
- Yuan T. T., Kewley L. J., Sanders D. B., 2010, *ApJ*, 709, 884
- Yuan S., Strauss M. A., Zakamska N. L., 2016, *MNRAS*, 462, 1603
- Zakamska N. L., 2010, *Nature*, 465, 60

Zakamska N. L., Gómez L., Strauss M. A., Krolik J. H., 2008, *AJ*, **136**,
1607

Zakamska N. L., et al., 2016, *MNRAS*, **455**, 4191

Zhang Y., Kwok S., 2015, *ApJ*, **798**, 37

This paper has been typeset from a $\text{\TeX}/\text{\LaTeX}$ file prepared by the author.